Optimising social mixing strategies to mitigate the impact of COVID-19 in six European countries: a mathematical modelling study

Supplementary Appendix

Romain Ragonnet, Guillaume Briffoteaux, Bridget M. Williams, Julian Savulescu, Matthew Segal, Milinda Abayawardana, Rosalind M. Eggo, Daniel Tuyttens, Nouredine Melab, Ben J. Marais, Emma S. McBryde, James M. Trauer

Contents

1 Model description

1.1 Base platform

We developed a deterministic compartmental model of SARS-CoV-2 transmission using the AuTuMN platform, publicly available at github.com/monash-emu/AuTuMN [1]. This repository allows for the rapid and robust creation and stratification of models of infectious disease epidemiology and includes pluggable modules to simulate heterogeneous population mixing, demographic processes, multiple circulating pathogen strains, repeated stratification and other modelling features relevant to infectious disease transmission.

1.2 Base model

For this application, we first created a model with sequential compartments representing susceptible (S), latently infected (E), infectious pre-symptomatic (P), early disease (I), late disease (L) and recovered (R) persons (although patients in the early and late disease compartments are not considered symptomatic if assigned to the first "clinical" stratification, as described in Section 1.4). The latently infected and infectious pre-symptomatic periods together comprise the incubation period, with the incubation period and the proportion of this period for which patients are infectious defined by parameters described below. The transition from early disease to late disease is intended to represent the point at which patients are detected (in the event that detection does eventually occur) and isolation then occurs from this point forward (i.e. applies during the late disease phase only). This transition point is also intended to represent the point of admission to hospital or to intensive care for patients for whom this occurs (again see Section 1.4).

When waning immunity was assumed, individuals transitioned back to a susceptible compartment at a rate that was defined as the reciprocal of the assumed immunity duration. The compartments S, E and P were stratified by infection history, such that differential risks of severe disease could be considered for individuals who have experienced SARS-CoV-2 infection before, compared to infection-naive individuals.

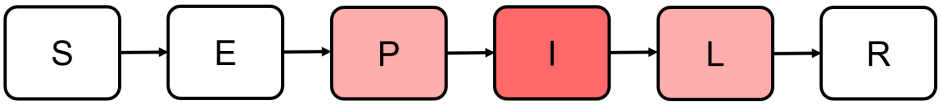

Figure S1. Compartmental structure of the base model.
Red shading indicates infectiousness.

1.3 Age stratification

All compartments of this base compartmental structure were stratified by age into five-year bands from 0-4 years of age through to 70-74 years of age, with the final age group being those aged 75 years and older.

We used the age-specific contact matrices by location (home, schools, workplace and other locations) reported by Prem *et al.* for the five investigated countries to inform heterogeneous mixing in our models [2]. The model age groups were chosen to match these mixing matrices. We did not implement births, ageing and non-COVID-19-related deaths given that the current study pertains to the short to medium-term and the immediate implementation of non-pharmaceutical interventions, for which population demographics are less relevant.

1.4 Clinical stratification

The age-stratified early and late disease compartments I and L were further stratified into five categories: 1) asymptomatic, 2) symptomatic ambulatory never detected, 3) symptomatic ambulatory ever detected, 4) hospitalised never critical and 5) ever critically unwell. The proportion of new infectious persons entering stratum 1 (asymptomatic) is age-dependent as described in Table S4. When waning immunity was assumed, these proportions also depended on the individuals' infection history, such that a smaller proportion of symptomatic infections may be considered for repeat episodes of SARS-CoV-2 infection. The proportion of symptomatic patients (strata 2 to 5) ever detected (strata 3 to 5) is set through a time-variant parameter that represents the proportion of all symptomatic patients who are ever detected. Of those ever symptomatic (strata 2 to 5), an age-specific proportion was considered to be hospitalised (entering strata 4 or 5). Of those hospitalised (entering strata 4 or 5), a fixed proportion was considered to be critically unwell (entering stratum 5). The figures below illustrate this conceptual approach.

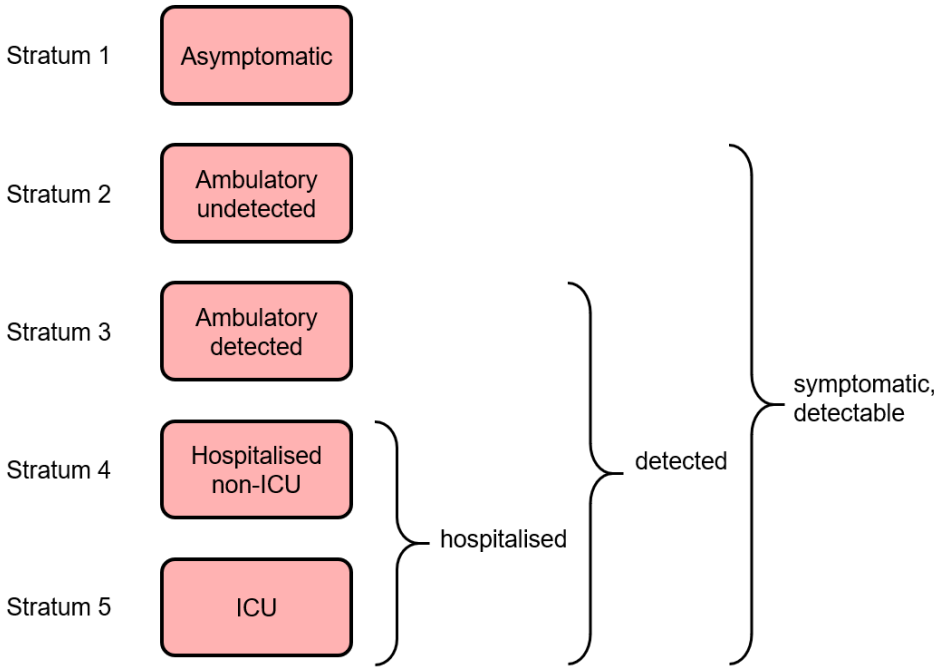

Figure S2. Clinical stratification applying to compartments I and L.

1.5 COVID-19-related death

We used age-specifc infection fatality rates (IFRs) to model COVID-19 deaths. These rates were derived by combining data from the recent Spanish nationwide seroprevalence survey, age-specific population sizes reported by the United Nations and mortality data reported by the Spanish Ministry of health [3,4]. The seroprevalence survey was conducted between 27 April and 11 May 2020. In order to account for the delay between disease onset and time of death, we used the total number of deaths reported on the 22 May's governmental report which included deaths up until 21 May 2020 (available here). This date was obtained by considering a 16 day delay from the survey period's midpoint (5 May 2020), relying on published estimates of times to deaths [5]. The age-specific IFRs

age (years)	% seropositive	number of deaths
0	0.0 (0.0-11.9)	
1-4	3.5 (1.7-6.8)	2
5-9	3.6 (2.3-5.7)	
10-14	4.1 (3.1-5.5)	5
15-19	3.8 (2.8-5.0)	
20-24	5.5 (4.3-7.0)	24
25-29	5.4 (4.1-7.1)	
30-34	4.3 (3.3-5.4)	63
35-39	4.8 (3.9-6.0)	
40-44	4.7 (3.9-5.7)	217
45-49	5.1 (4.2-6.2)	
50-54	4.9 (4.0-5.9)	657
55-59	4.9 (4.1-5.9)	
60-64	4.1 (3.3-5.2)	1822
65-69	4.9 (3.8-6.3)	
70-74	4.6 (3.5-5.9)	4887
75-79	4.2 (3.0-5.9)	
80-84	5.0 (3.4-7.4)	8458
85-89	3.6 (2.1-6.1)	
90+	2.4 (1.1-5.3)	4417

Table S1. Age-specific estimates of seropositive proportions and numbers of deaths in Spain.
% seropositive corresponds to the results obtained based on the immunoassay test in Pollan *et al.* The numbers of deaths include deaths until 21 May 2020 inclusive.

were obtained from:

$$IFR_i = \frac{d_i}{p_i \pi_i}, \tag{1}$$

where IFR_i is the IFR of age-group i, d_i is the total number of deaths observed in age-group i until 21 May 2020, p_i is the proportion of seropositive individuals among age-group i and π_i is the size of the population of age-group i.

Table S1 summarises the data used to calculate the age-specific IFRs and the resulting IFR estimates are presented in Table S4. The confidence intervals presented in Table S4 were obtained by substituting p_i with the 95% bounds of the estimates of seroprevalence in Equation 1. We then doubled the widths of these intervals when defining the IFRs' prior distributions (Table S3), as we recognise that there may be other sources of uncertainty than those considered in our estimation. These includes uncertainties in the reported numbers of deaths or the fact that IFRs may vary by country.

The IFRs were distributed across strata 4 and 5, with no deaths applied to the first three strata. If the infection fatality rate was greater than half of the absolute proportion of persons critically unwell (entering stratum 5), the proportion of critically unwell persons dying was set at 50% and the remainder of the infection fatality rate was applied to the hospitalised proportion. Otherwise, if the infection fatality rate was less than half of the absolute proportion of persons critically unwell, the IFR was applied entirely through stratum 5 (such that the proportion of critically unwell persons dying in that age group is then less than 50% and the proportion of stratum 4 dying was set to zero).

Clinical stratum	Pre-symptomatic	Early disease	Late disease
Asymptomatic	0.7	0.7	0.7
Ambulatory undetected	0.7	1	1
Ambulatory detected	0.7	1	0.2
Hospitalised non-ICU	0.7	1	0.2
ICU	0.7	1	0.2

Table S2. Illustration of the relative infectiousness of disease compartments by clinical stratification and stage of infection.
Darker shades of red indicate higher levels of infectiousness.

1.6 Infectiousness

For patients with disease who were admitted to hospital, the sojourn time in the early and late infectious compartments was modified, as indicated in Table S3. The point of admission to hospital was considered to be the transition from early to late infectious disease, such that the sojourn time in late disease was the period of time admitted to hospital. For patients admitted to ICU, admission to hospital and admission to ICU occurred at this same point. Infectiousness declined at the point of transition from early to late disease for all patients admitted to hospital (both ICU and non-ICU) and for patients who were effectively detected and so underwent isolation. The relative infectiousness of both early and late compartments within the asymptomatic stratum, as well as the late disease compartment of the symptomatic ambulatory detected late disease were modified. This was intended to reflect lower infectiousness per unit time of asymptomatic persons and of detected persons who were assumed to self-isolate from the point of entering the late disease compartment. Pre-symptomatic individuals were assumed to have the same level of infectiousness as asymptomatic diseased individuals. Persons with late stage disease in the hospital and critical strata also had their infectiousness modified. Table S2 illustrates the different levels of infectiousness associated with the different clinical strata and the different infection stages.

1.7 Implementation of non-pharmaceutical interventions

For this study, it was critical to simulate the past dynamics of the epidemics accurately in order to capture the level of immunity acquired in the past. For this reason, we needed to capture the past impact of non-pharmaceutical interventions (NPIs) such as social distancing or school closures.

1.7.1 Isolation and quarantine

For persons who are identified with symptomatic disease and enter clinical stratum 3, self-isolation is assumed to occur. The proportion of ambulatory symptomatic persons effectively identified through the public health response by any means is set by the time-variant process described in Section 1.7.2. On moving to stratum 3, infectiousness declines according to the "relative infectiousness of identified persons undergoing quarantine and isolation" parameter indicated above.

1.7.2 Modelling time-variant detection

The proportion of symptomatic individuals detected was varied over time in order to account for increasing detection during the course of the epidemic. We used the following

translated and rescaled logistic function to model this increase:

$$prop_{sympt\_detected}(t) = prop_{start} + \frac{prop_{final} - prop_{start}}{2} \left(tanh\left(b\left(t - c\right)\right) + 1\right),$$

where $prop_{start}$ is the proportion of symptomatic individuals that are detected at the start of 2020, $prop_{final}$ is the maximum asymptotic proportion of symptomatic individuals that are detected, b is a shape parameter defining how rapidly scaling occurs and c is the time when inflection occurs in the scale-up curve. The parameters $prop_{final}$, b and c are automatically estimated during model calibration (see Section 2). Figure S3 illustrates two examples of functions describing the proportion of symptomatic individuals that are detected over time. The six countries' detection profiles inferred from the detection parameters' posterior distributions are presented in Section 2.5.

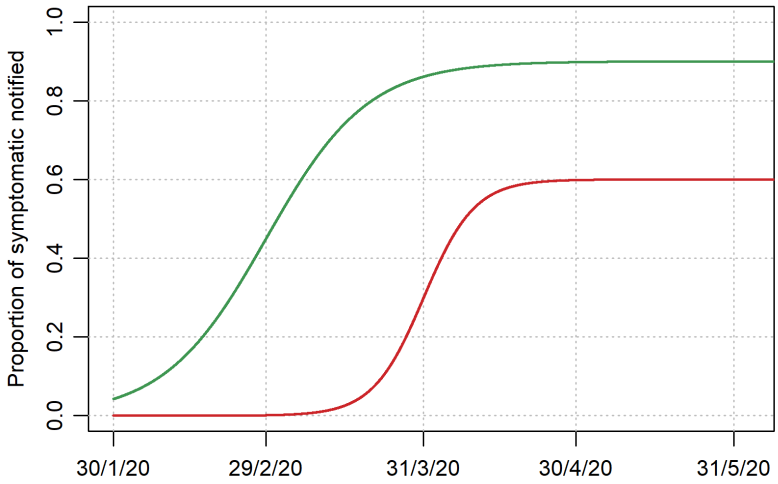

Figure S3. Examples of modelled time-variant proportions of symptomatic individuals detected over time.
Two parameter sets are illustrated: ($prop_{start} = 0$, $prop_{final} = 0.6$, $b = 0.1$, $c = 31/3/2020$) in red; ($prop_{start} = 0$, $prop_{final} = 0.9$, $b = 0.05$, $c = 29/2/2020$) in green.

1.7.3 Other non-pharmaceutical interventions

For all NPIs relating to reduction of human mobility or "lockdown" (i.e. all NPIs other than isolation and quarantine), these interventions are implemented through dynamic adjustments to the age-assortative mixing matrix. The mixing matrices of Prem et al. allow for disaggregation of total contact rates by location, i.e. home, work, school and other locations. This disaggregation allows for the simulation of various NPIs in a local context by dynamically varying the contribution of each location to reflect the historical implementation of the interventions. The corresponding mixing matrix (denoted C_0) is presented using the standard convention that a row represents the average numbers of age-specific contacts per day for a contact recipient of a given age-group. In other words, the element $C_0[i, j]$ is the average number of contacts per day that an individual of age-group i has with individuals of age-group j. This matrix results from the summation of the four context-specific contact matrices: $C_0 = C_H + C_S + C_W + C_L$, where C_H, C_S, C_W and C_L are the age-specific contact matrices associated with households, schools, workplaces and

other locations, respectively. In our model, the contributions of the matrices C_S, C_W and C_L are time-variant, such that the input contact matrix can be written:

$$C(t) = C_H + s(t)C_S + w(t)C_W + l(t)C_L, \tag{2}$$

where s, w and l are location-specific time-variant multipliers. The following three sections describe how these multipliers are set and Figure S4 shows their respective profiles for the six countries.

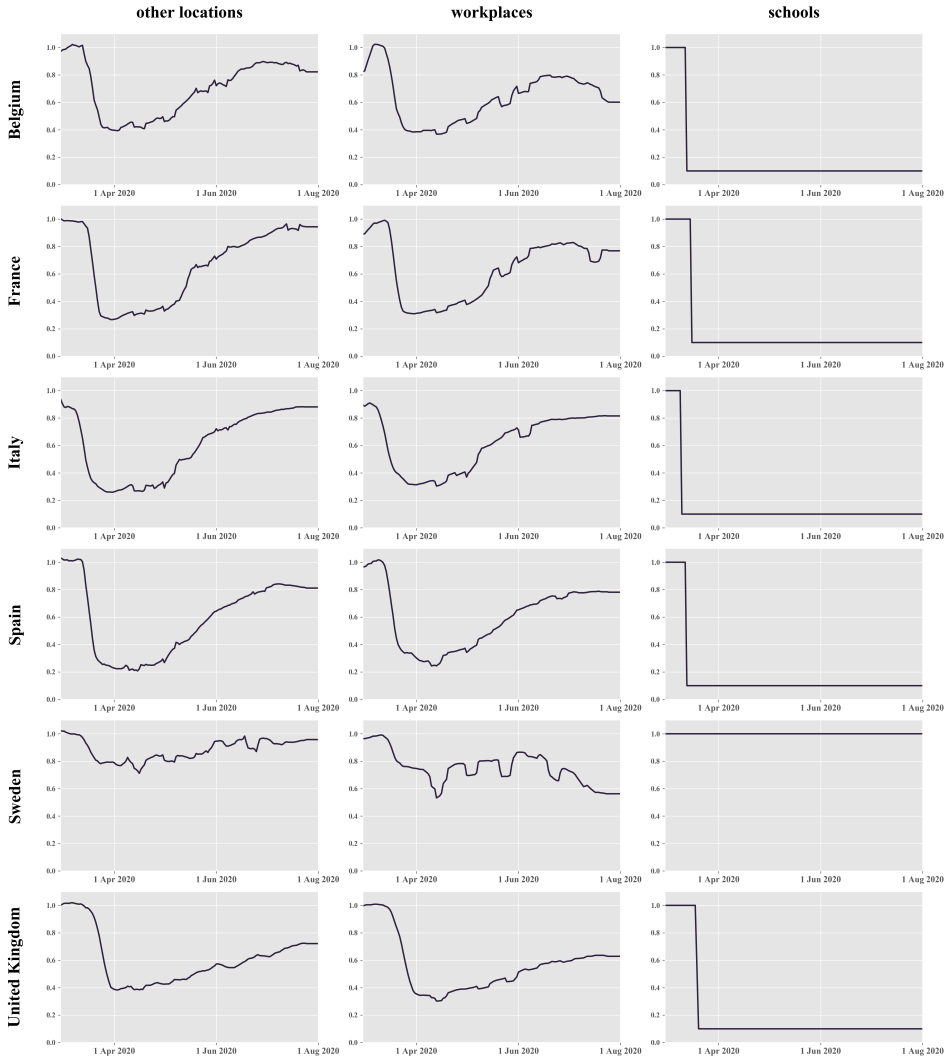

Figure S4. Time-variant contact rate multipliers used to model mobility restrictions. "Other locations" refers to all places other than schools, workplaces or households.

It is important to note that s, w, l are all set back to 1 when predicting the future epidemic during Phase 3 as well as during Phase 2 when mixing is optimised by age (see Section 3 for description of the different phases).

School closures

School closures were represented by decreasing the contribution of the school-based contacts to the mixing matrix by 90% at the time school closures occurred in the country considered. The closure times were obtained from the UNESCO website [6]. The reason why the school contacts were not set to zero after closure is that many schools continued

to accept some children whose parents worked in priority sectors.

Workplace closures
Workplace closures were represented by proportionally reducing the contribution of workplace contacts to the total mixing matrix over time. We used Google mobility data to inform this time-variant proportional reduction after applying a 7-day moving average to the raw data [7].

Community-wide movement restriction
This was simulated by reducing the contribution of the "other location" contacts to the overall mixing matrix. The functional form of this reduction was set using Google mobility data and obtained by combining the proportional reductions reported by Google for the three categories "Retail and recreation", "Supermarket and pharmacy" and "Public transport" [7]. We did not include the relative changes of the "Parks" category, as their contribution to transmission is expected to be minimal. The proportional reduction applied to the "other locations" contact rates $\rho := 1 - l$, was obtained from:

$$\rho(t) = \frac{\rho_R(t) + \rho_S(t) + \rho_P(t)}{3},$$

where ρ_R, ρ_S and ρ_P are the proportional reductions reported by Google for "Retail and recreation", "Supermarket and pharmacy" and "Public transport", respectively. We applied a 7-day moving average to the raw data for smoothing.

Micro-distancing
The previous adjustments to social mixing reflected reductions in people's mobility that resulted in lower rates of contact. In addition to this, we apply a time-variant reduction to the per-contact probability of transmission. This adjustment is referred to as micro-distancing and is intended to capture physical distancing between individuals, mask wearing and other preventive measures that individuals may take to reduce the per-contact transmission risk. Micro-distancing was modelled using a decreasing function of time to describe the transmission probability multiplier. It was implemented as:

$$m_d(t) = 1 - \frac{1 - micro_{final}}{2} \left(tanh\left(-0.05\left(t - micro_{inflection}\right)\right) + 1 \right),$$

where $micro_{final}$ represents the final value of the transmission probability multiplier and $micro_{inflection}$ is the time when inflection occurs in the scaling curve. Figure S5 illustrates two examples of micro-distancing profiles. Note that the parameters $micro_{final}$ and $micro_{inflection}$ were automatically inferred during calibration.

1.8 Model equations

The dynamics of the model are governed by a set of ordinary differential equations. We use the subscripts a, h and c to denote the different age-groups, the two infection history statuses and the clinical strata, respectively. That is, a is an element of {"0-4", "5-9", ..., "70-74", "75+"}, h is an element of {"infection-naive", "previously infected") } and c is one of {"asymptomatic", "ambulatory undetected", "ambulatory detected", "hospitalised non-ICU", "ICU"}.

Using the compartment notation introduced in Section 1.2 and the parameter notation

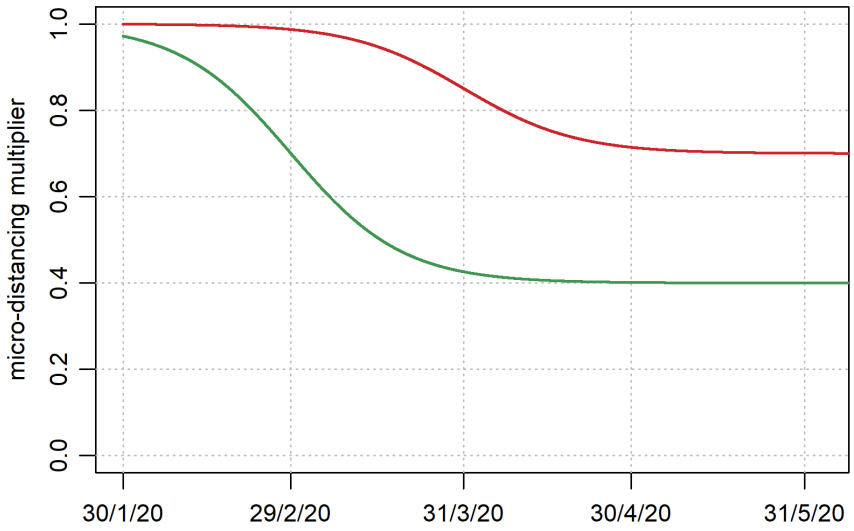

Figure S5. Examples of time-variant micro-distancing profiles.
Two parameter sets are illustrated: ($micro_{final} = 0.7$, $micro_{inflection} = 31/3/2020$) in red; ($micro_{final} = 0.4$, $micro_{inflection} = 29/2/2020$) in green.

presented in Table S5, we have:

$$\begin{cases} \dot{S}_{a,h} &= -\lambda_a(t)\sigma_a S_{a,h} + \omega R_a \mathbb{1}_{\{h=\text{“previously infected”}\}} \\ \dot{E}_{a,h} &= \lambda_a(t)\sigma_a S_{a,h} - \alpha E_{a,h} \\ \dot{P}_{a,h} &= \alpha E_{a,h} - \nu P_{a,h} \\ \dot{I}_{a,c} &= \sum_h p_{a,h,c}(t)\, \nu P_{a,h} - \gamma_c I_{a,c} \\ \dot{L}_{a,c} &= \gamma_c I_{a,c} - \delta_{a,c} L_{a,c} - \mu_{a,c} L_{a,c} \\ \dot{R}_a &= \sum_c \delta_{a,c} L_{a,c} - \omega R_a \quad , \end{cases} \tag{3}$$

where:

$$\begin{cases} \lambda_a(t) &= \beta \times m_d(t) \left[\sum_j \frac{\epsilon \times P_j}{N_j} C_{a,j}(t) \; + \; \sum_{j,c} \frac{\iota_c \times I_{j,c} + \kappa_c \times L_{j,c}}{N_j} C_{a,j}(t) \right], \\ \sum_c p_{a,h,c}(t) &= 1, \quad \forall t \in \mathbb{R}, \; \forall h \in \{\text{“}infection-naive\text{”}, \text{“}previously\ infected\text{”}\}. \end{cases} \tag{4}$$

Parameter	Definition	Value/range	Source
Epidemic seeding time*,[c]	Time when first infectious individuals were introduced in the model	0 - 40	Assumption
Transmission probability per contact[c]	Probability of transmission per contact between a fully-infectious and a fully-susceptible individual	0.02 - 0.06	Early model explorations
Incubation time[c]	Average total duration spent in pre-disease infection compartments (E and P)	3 - 7 days	[8–11]
Incubation infectious proportion	Proportion of incubation period infectious	0.5	[12]
Disease duration[c]	Average total duration spent in the disease compartments (I and L). Does not apply to hospitalised patients.	4 - 10 days	[11]
Early disease proportion (non-hospital)	Proportion of disease period before isolation can occur for individuals who are never hospitalised	0.33	Assumed (i.e. that identification and isolation can only occur after the first third of the disease episode has elapsed)
Early disease duration (hospital non-ICU)	Disease duration prior to admission for hospitalised patients not critically unwell	8.1 days	Expected mean from ISARIC cohort, as reported on 8th June 2020 [13]
Early disease duration (ICU)	Disease duration prior to admission for ICU patients	12.7 days	Calculated as 8.1 days prior to hospital admission plus 4.6 days in hospital prior to ICU admission. Former value being as for disease duration prior to admission for hospitalised patients not critically unwell. Latter value being expected mean of period from admission to ICU entry from ISARIC cohort, as reported on 8th June 2020 [13].
Late disease duration (hospital)[c]	Average hospitalisation duration, excluding ICU	17.7 - 20.4 days	Expected mean from ISARIC cohort, as reported on 8th June 2020. [13]
Late disease duration (ICU)[c]	Average duration in intensive care unit	9 - 13 days	Mean duration of stay in ICU/HDU from ISARIC cohort, as reported on 8th June 2020 [13]
Symptomatic proportions uncertainty[c]	Multiplier applying to the age-specific proportions of symptomatic presented in Table S4	0.6 - 1.4	Assumption
Hospital proportions uncertainty[c]	Multiplier applying to the age-specific proportions of hospitalised presented in Table S4	0.6 - 1.4	Assumption
ICU proportion[c]	Proportion of hospitalised individuals admitted to intensive care	0.15 - 0.20	[13]
Infection fatality rates[c]	Age-specific proportions of death among infected individuals (9 parameters varied independently)	See Table S4	Pollan *et al.* [3] Spanish Ministry of Health [4]
Detection profile: $\rightarrow prop_{start}$[c] $\rightarrow prop_{final}$[c] $\rightarrow b$[c] $\rightarrow c$*,[c]	See Section 1.7.2.	 0 - 0.10 0.10 - 0.90 0.05 - 0.10 70 - 160	Assumption
Micro-distancing: $\rightarrow micro_{final}$[c] $\rightarrow micro_{inflection}$*,[c]	See Section 1.7.3	 0.40 - 0.75 80 - 130	Assumption

Table S3. Model parameters.
*times are expressed as number of days since 31 December 2019. [c]Parameter included in the MCMC calibration.

Age group	Proportion symptomatic[u]	Relative susceptibility to infection	Proportion of symptomatic patients hospitalised[u]	Infection fatality rate
0-9	0.29	0.4	0.001	$1.35e^{-5}$ ($1.07e^{-5} - 1.81e^{-5}$)
10-19	0.21	0.38	0.003	$2.7e^{-5}$ ($2.4e^{-5} - 3.1e^{-5}$)
20-29	0.27	0.79	0.012	$9.5e^{-5}$ ($8.5e^{-5} - 0.00011$)
30-39	0.33	0.86	0.032	$2.3e^{-4}$ ($2.1e^{-4} - 2.6e^{-4}$)
40-49	0.40	0.80	0.049	$5.6e^{-4}$ ($5.1e^{-4} - 6.1e^{-4}$)
50-59	0.49	0.82	0.102	$1.9e^{-3}$ ($1.7e^{-3} - 2.1e^{-3}$)
60-69	0.63	0.88	0.166	$7.7e^{-3}$ ($6.9e^{-3} - 8.6e^{-3}$)
70-79	0.69	0.74	0.243	0.027 (0.024 − 0.032)
80 and above	0.69	0.74	0.273	0.11 (0.09 − 0.13)
Source	Davies *et al.* 2020 [14]	Davies *et al.* 2020 [14]	Verity *et al.* 2020 [15]	Pollan *et al.* [3] Spanish Ministry of Health [4]

Table S4. Age-specific parameters.
[u]Uncertainty was incorporated around this parameter by applying a multiplier that was varied in the MCMC (see Table S3).

parameter	definition
σ_a	relative susceptibility to infection by age
α	rate of progression from latent to pre-symptomatic state
ν	rate of progression from pre-symptomatic to early disease state
$p_{a,c}$	age-specific proportion progressing to each clinical stratification
γ_c	rate of progression from early active disease to late active disease
$\delta_{a,c}$	rate of progression from late active disease to recovered state
ω	rate of immunity loss
$\mu_{a,c}$	rate of COVID-19-related mortality
β	probability of infection per contact between a fully-infectious and a fully-susceptible individual
m_d	time-variant multiplier used to model micro-distancing (Section 1.7.3)
ϵ	relative infectiousness of pre-symptomatic individuals
ι_c	clinical stratification infectiousness vector for early disease compartments
κ_c	clinical stratification infectiousness vector for late disease compartments
$C_{a,j}$	contact matrix element $[a, j]$, defined as the average daily number of persons of age a contacted by an individual of age j.

Table S5. Parameter notation for ordinary differential equations.

2 Model calibration

The model was calibrated using a Markov Chain Monte Carlo algorithm (MCMC). In particular, we used the Metropolis-Hastings algorithm with Gaussian proposal functions to sample parameters from their posterior distributions. For each country, we ran 7 independent MCMC chains initialised using Latin Hypercube Sampling based on the parameter priors. We ran simulations for 3 hours per chain in order to achieve at least 2,500 iterations per chain. We discarded the first 1,000 iterations of each chain as burn-in and combined the samples of the 7 chains to project epidemic trajectories over time. The definitions of the prior distributions and the likelihood are detailed in the following sections.

2.1 Parameters varied during calibration

The parameters varied during the MCMC calibration along with their associated prior ranges are listed in Table S3 and indicated with the superscript ^{c}. We used uniform prior distributions to reflect the still limited knowledge about SARS-CoV-2 epidemiology.

2.2 Calibration targets

We used the data reported by the World Health Organization for the daily numbers of COVID-19 confirmed cases between 1 March 2020 and 15 July 2020 in the six countries considered [16]. We then converted the daily counts into weekly totals in order to remove the effect of weekdays versus weekends in cases reporting. We also used hospitalisation data as calibration targets. We fitted the model to daily numbers of new hospitalisations (7-day average) when these data were available (Belgium, France, Spain, UK). In contrast, the daily number of patients currently hospitalised was used for Italy, and the daily number of new patients in intensive care units were used for Sweden. The sources of the hospitalisation data are summarised in Table S6 and the data points used for calibrations are presented in Figure S6.

Country	**Hospitalisation indicator**	**Source**
Belgium	New hospital admissions	COVID-19 Belgium Epidemiological Situation dashboard [17]
France	New hospital admissions	data.gouv.fr platform (French Government) [18]
Italy	Current total of hospitalisations	National COVID-19 data repository [19]
Spain	New hospital admissions	Spanish Ministry of Health [4]
Sweden	New ICU admissions	Swedish Intensive Care Registry [20]
United Kingdom	New hospital admissions	COVID-19 Government dashboard [21]

Table S6. Summary of hospital data used to calibrate the models.

2.3 Likelihood calculation

Let n_i denote the average daily number of new confirmed COVID-19 cases in a given country during week i, and ν_i^θ the associated predicted number according to the model when using the parameter set θ. Similarly, let us denote h_i as the average daily number of new COVID-19 hospitalisations (or average daily hospital occupancy for Italy, or average daily number of new ICU admissions for Sweden) during week i, and δ_i^θ the associated predicted number according to the model when using the parameter set θ. The MCMC likelihood was defined as follows:

$$\mathcal{L}(\theta) := \prod_i f(n_i|\, \nu_i^\theta,\, \sigma_n) \times f(h_i|\, \delta_i^\theta,\, \sigma_h),$$

where $f(.|\, \mu,\, \sigma)$ is the probability mass function of the normal distribution with mean μ and standard deviation σ. The parameters σ_n and σ_h were automatically estimated by the MCMC.

2.4 Fitted model

Figure S6 shows our model projections against local data for case notifications and the hospital-related indicators used for each country's model calibration. We also present the posterior estimates of proportion of recovered individuals over time in Figure S7. In this figure, we also show estimates of antibody prevalence from sero-prevalence surveys for comparison. Note that these estimates were not include as calibration targets. Table S7 provides details about the reported sero-prevalence estimates.

Country	Population	Sampling	Approach	Date	Result	Source
Belgium	Nationwide	Convenience	Residual sera taken outside hospitals by diagnostic laboratories.	30 Mar - 5 Apr 2020 20-26 Apr 2020 18 - 25 May 2020 8 - 13 Jun 2020 29 Jun - 3 Jul 2020	2.9% (2.3 - 3.4) 6.0% (5.1 - 7.1) 6.9% (5.9 - 8.0) 5.5% (4.7 - 6.5) 4.5% (3.7 - 5.4)	[22]
France	Four department areas	Convenience	Blood donor samples assessed with virus neutralisation assay	Last week of March & first week of April 2020	2.71%	[23]
Italy	Nationwide	Stratified, two-stage sampling	Home-based collection of serum	25 May - 15 Jul 2020	2.5%	[24]
Spain	Nationwide	Random, stratified, two-stage	Fingerprick RDT, and CLIA on serum	27 Apr - 11 May 2020 18 May - 1 Jun 2020 8 - 22 jun 2020	5.0% (4.7 - 5.4) 5.2% (4.9 - 5.5) 5.2% (4.9 - 5.5)	[3]
Sweden	Stockholm urban area	Random	Home-sampled DBS asses with multiplex serology assay.	May 2020	10.8% (7.9%-13.7%)	[25]
United Kingdom	Nationwide	Representative sample	Biobank participants, self-collected fingerprick sample tested with ELISA	27 Apr - 3 May 2020	7.1%	[26]
United Kingdom	Nationwide	Random	Self-administeered lateral flow immunoassay	20 Jun - 13 Jul 2020	6.0% (5.8, 6.1)	[27]

Table S7. Survey estimates of seroprevalence for the six analysed countries. The numbers in brackets represent 95% confidence intervals.

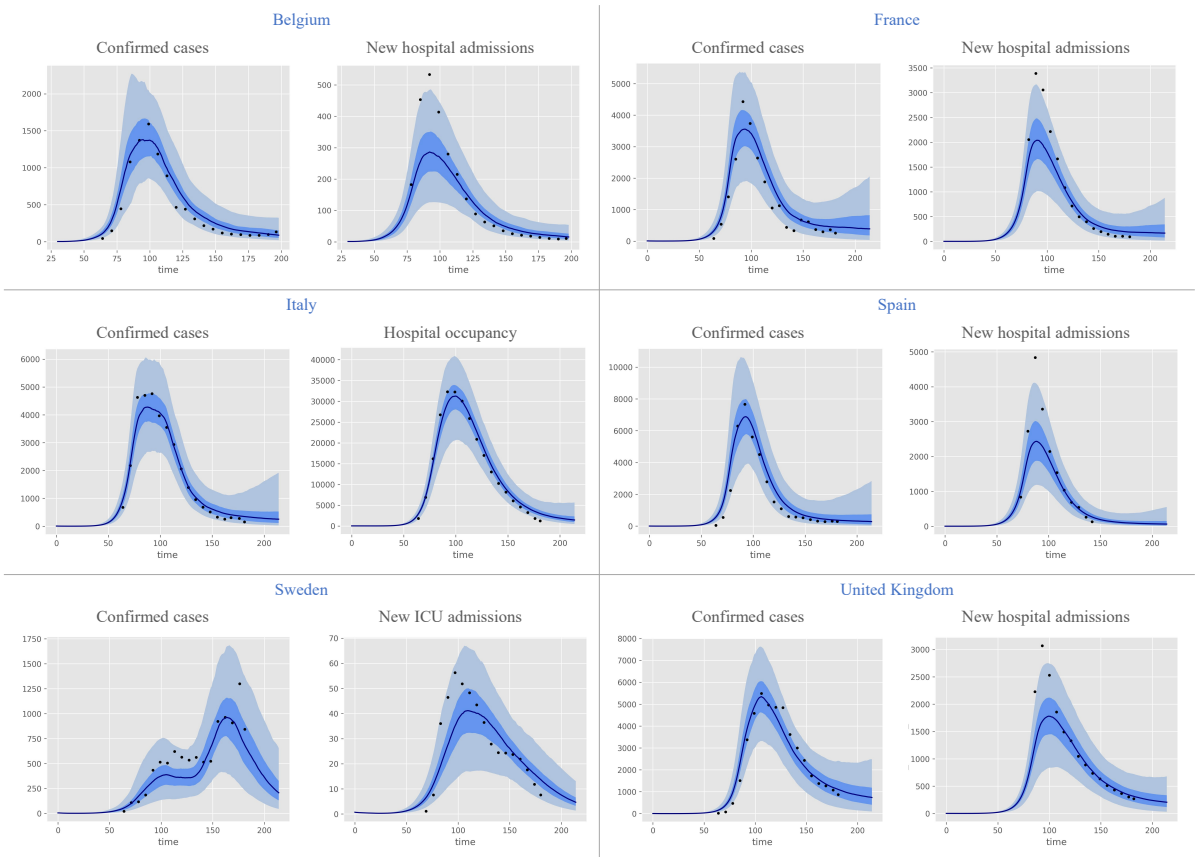

Figure S6. Model projections compared against local data.
The figures present the median estimates (dark blue line) and the central 95% credible intervals (light blue shade) against observed numbers of confirmed COVID-19 cases and hospitalisations (black dots). The x-axis represents the time in days since 31/12/2019. Values on the y-axis are daily numbers of confirmed cases or hospitalisations. The data points represent the weekly average of the daily counts.

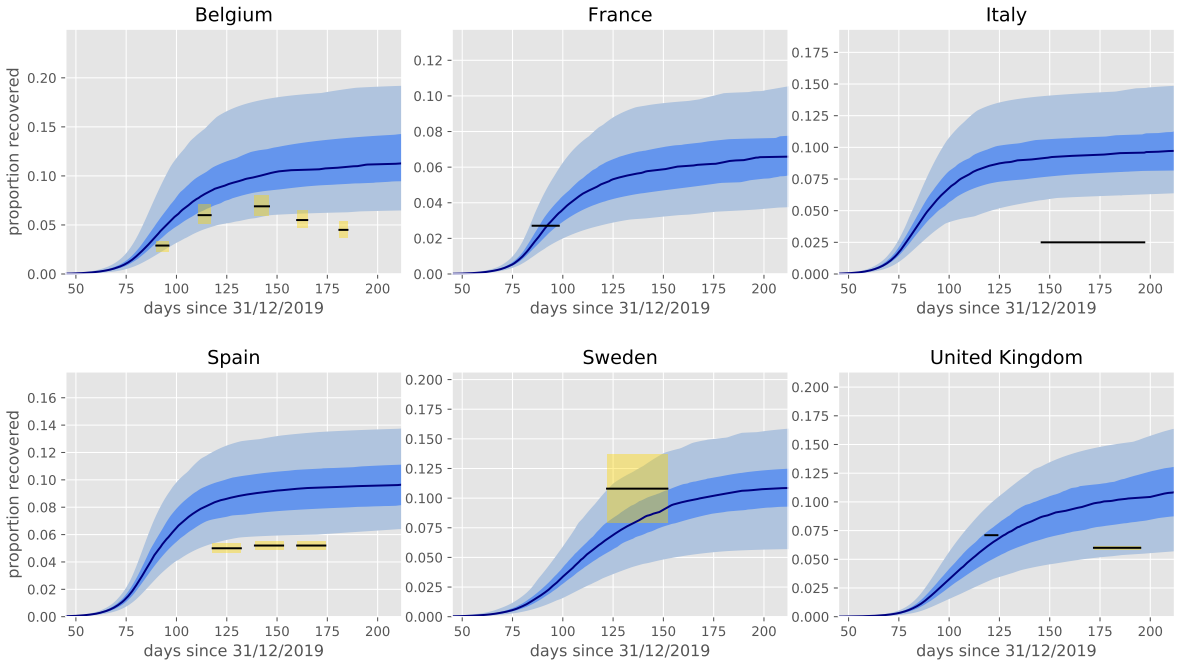

Figure S7. Model projections of proportion of recovered individuals over time. The figures present the median estimates (dark blue line), the interquartile range (dark blue shade) and the central 95% credible intervals (light blue shade) of the proportion of recovered individuals over time. The x-axis represents the time in days since 31/12/2019. Estimates of antibody prevalence obtained from sero-prevalence surveys are also shown (yellow boxes and black lines). The horizontal span of the boxes/lines represent the survey periods. The vertical span shows the 95% confidence interval, when available.

2.5 Parameters' posterior distributions

The posterior distributions of the parameters listed in Table S3 are presented in Figure S8. The ranges used on the x-axes correspond to the intervals used to define the parameters' prior distributions.

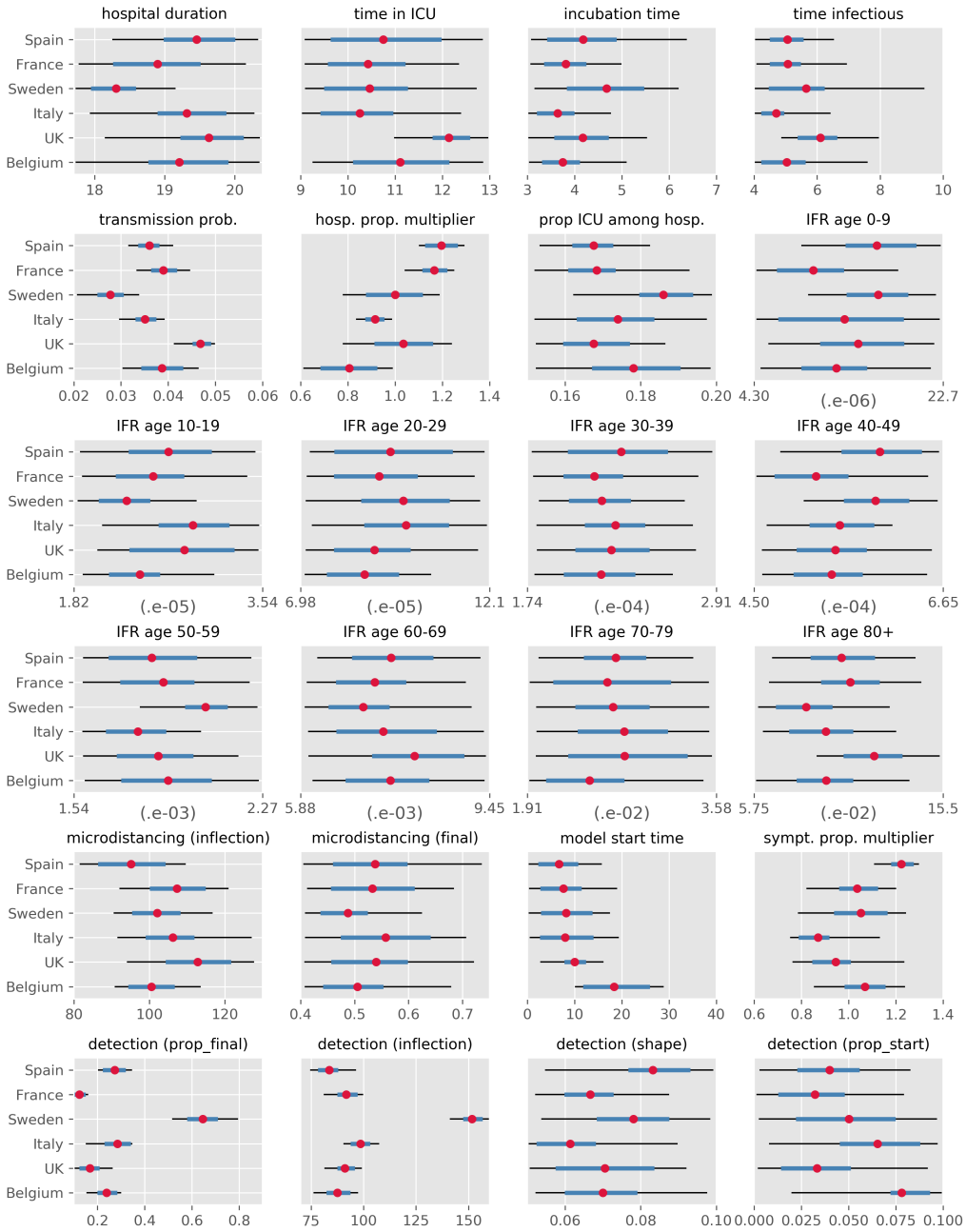

Figure S8. Posterior estimates of model parameters.
The mean estimates are represented with a red dot. The central 50% credible intervals are shown in blue and the central 95% credible interval are represented with black bars.

Using the posterior samples of the detection parameters, we computed estimated profiles of the time-variant proportion of symptomatic detected. The six countries' detection profiles are shown in Figure S9.

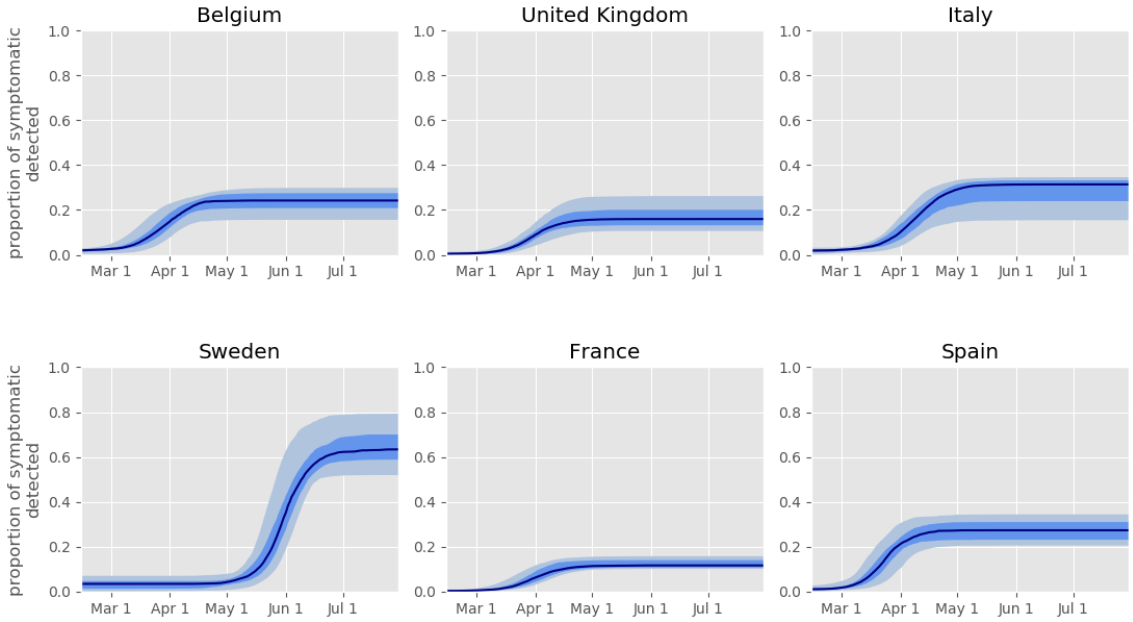

Figure S9. Posterior estimates of the time-variant proportion of symptomatic persons detected.
The figures present the median estimate (black line), central 50% credible interval (dark blue) and central 95% credible interval (light blue).

3 The three simulation phases

The model is used to simulate three successive phases that have different purposes:

1. Modelling the past (until 31 July 2020),
2. Mitigating the age-specific or location-specific social mixing (during 6 or 12 months from 1 August 2020),
3. Relaxing all restrictions and testing for herd immunity (until 31 October 2021).

Figure 1 (main text) illustrates these three phases, both in the presence and in absence of herd-immunity.

3.1 Phase 1: Modelling the past

This phase aims to simulate the past SARS-CoV-2 epidemic accurately in order to capture the level of immunity acquired by August 2020. During this phase which ends on 31th July 2020, model parameters were automatically calibrated in order for the model predictions to match the numbers of notified COVID-19 cases and hospitalisations. Our Bayesian approach to calibration also allowed us to account for uncertainty in the model inputs. This approach is described in Section 2.

3.2 Phase 2: Mitigating the age-specific or location-specific social mixing

The second simulation phase begins on the 1st of August 2020 and lasts 6 or 12 months depending on the configuration considered. It is during this phase that the social mixing profile was varied and optimised.

Optimisation performed by adjusting mixing by age

In a first analysis, we aimed to find the optimal age-specific adjustments to the contact matrix. Under this scenario, the location-specific multipliers $s(t)$, $w(t)$ and $l(t)$ described in Equation 2 were all set back to 1, so was the micro-distancing multiplier. All the other parameter values remained the same as those used during Phase 1, including for the parameters that are automatically calibrated (Section 2). In addition, we used age-specific multipliers that were varied during optimisation in order to model various strategies of mitigation by age.

Let us denote $m_i \in [0, 1]$ a relative mixing multiplier associated with age group $i \in \{1, ..., 16\}$. During Phase 2, we apply the adjusted contact matrix A defined by:

$$A[i, j] = m_i m_j C_0[i, j],$$

where C_0 is the original contact matrix provided by Prem *et al.* and described in Section 1.7.3. Note that during Phase 2, the matrix A replaced the matrix C in the equations presented in Section 1.8. We aimed to identify a combination $\{m_i, i \in \{1, ..., 16\}\}$ that:

1. leads to herd immunity by the end of Phase 2 and
2. minimises the mortality-related objective.

In Figure S10, we show the age-specific contributions in terms of total number of social contacts towards the elderly population. The contribution of age-group j in terms of contacts towards the age-group i was calculated as $C_0[i, j] \times \pi_j$, where π_j is the population of age-group j. These quantities are presented to help understand the optimised mixing profiles presented in the main text.

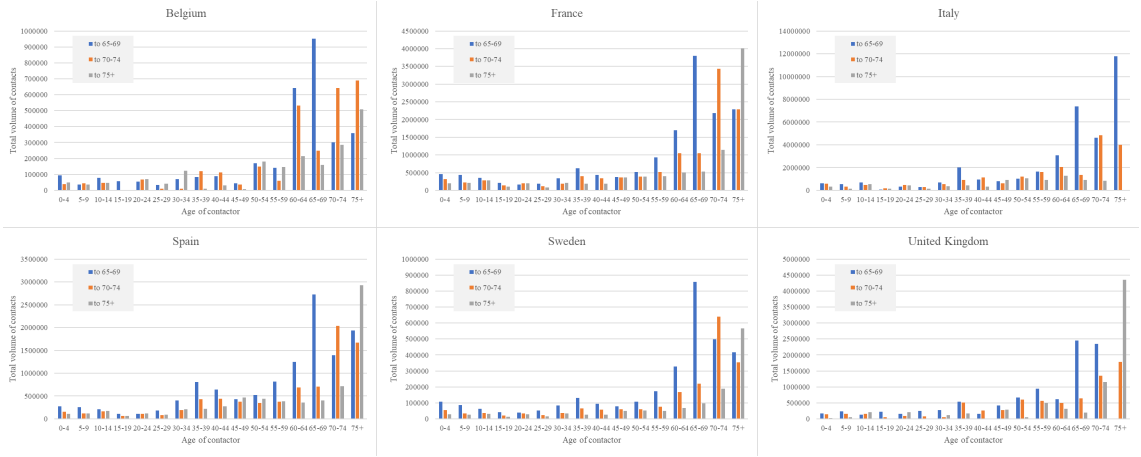

Figure S10. Age-specific contributions in terms of total number of contacts towards the elderly population.

Optimisation performed by adjusting mixing by location

In a separate exercise, we performed optimisation of social mitigation by location. Namely, we aimed to identify the optimal combinations of contact rate reductions in the three following locations: schools, workplaces and places other than schools, workplaces and homes. The rates of contacts occurring between household members were assumed to remain unchanged during this exercise. We aimed to achieve the same goals as with social

mitigation by age. Using the notation introduced in Equation 2, the decision variables of the optimisation problem become the location-specific multipliers $s(t)$, $w(t)$ and $l(t)$ that we consider constant during Phase 2.

The mortality-related objectives to minimise

We considered two different mortality-related objectives separately in this study. First, the optimisation exercise aimed to minimise the total number of deaths occurring during Phases 2 and 3. Then, we repeated all analyses by minimising the total number of life-years lost during the same period. The number of life-years lost was estimated by summing the expected number of remaining years that individuals would have lived if they had not died from COVID-19. This process was informed by the country-specific life-expectancy values by age reported by the United Nations.

3.3 Phase 3: Relaxing all restrictions and testing herd immunity

In this analysis, we were only interested in the strategies of mitigation by age that result in herd immunity by the end of Phase 2. We used a simulation-based approach to test whether herd immunity was reached at that time. To do this, we set all the age-specific mixing multipliers m_i and the location-specific multipliers s, w and l back to 1 at the start of Phase 3 in order to simulate an unmitigated epidemic. We assumed that herd immunity was reached by the end of Phase 2 if and only if the number of new diseased individuals was consistently found to decrease during Phase 3.

4 Optimisation of the age-specific social mixing

4.1 Problem description

Optimisation by age

For each country and for each configuration, we aimed to identify optimal combinations of the age-specific multipliers m_i described in Section 3. Let us denote $\Phi = \{m_1, \ldots, m_{16}\} \in [0, 1]^{16}$ a combination of these age-specific multipliers. Let also $\Psi(\Phi)$ be the associated mortality-related objective (either total numbers of deaths or life-years lost during Phases 2 and 3), and $H(\Phi)$ a binary variable indicating whether herd immunity has been achieved by the end of Phase 2 ($H(\Phi) = 1$ if herd immunity, 0 otherwise). We aimed to find Φ^* such that:

$$\Phi^* = \arg\min_{\Phi} \Psi(\Phi)\,, \tag{5}$$

$$\text{subject to: } H(\Phi) = 1\,. \tag{6}$$

Optimisation by location

The optimisation by location was defined in the same way as the optimisation by age except that the decision variables were the location-specific multipliers s, w and l described in Section 1.7.3 instead of the age-specific multipliers m_i.

4.2 Technical description of the optimisation algorithm

A total of 48 optimisations searches were performed, as we considered 6 countries, two different Phase 2 durations (6 and 12 months), two different objectives to minimise (deaths

and YLLs), and two optimisation modes (by age and by location). The optimisation exercises were treated independently using a parallel mono-objective Evolutionary Algorithm (EA) [28]. In an EA, a population of combinations is evolved by selection and reproduction of promising combinations already simulated (parents). The new combinations (children) generated by the reproduction operators are then simulated and replace the less promising combinations into the population.

The constraint of achieving herd immunity presented in Equation 6 was integrated into the mortality-related objective by setting the objective value to 8,000,000,000. This number is overwhelmingly greater than both the total number of possible deaths and the total number of possible life-years lost for all the countries considered in this study.

The parallel EA is described in Algorithm 1. The population of N combinations was initialized using Latin Hypercube Sampling and was then simulated in parallel (line 1 and 2). Within the generational loop (line 4 to 11), a population of parents was created by selecting N combinations from the population. The tournament selection of size 2 (line 5) repeatedly sampled 2 combinations with replacement from the population and retained the best one as parent. Parent characteristics were mixed by the SBX crossover operator [29] to generate the population of children (line 6). Children are next slightly modified by the polynomial mutation operator [29] and simulated in parallel (line 7 and 8). The best combinations from the population and the children were retained to form the new population (line 9).

Algorithm 1 Parallel Evolutionary Algorithm

Input
N: population size
budget: budget for the search

1: $\mathcal{P} \leftarrow$ LHS_sampling(N) ▷ initial population
2: parallel_simulation($\mathcal{P}$)
3: ($\boldsymbol{x}_{min}$, y_{min}) $\leftarrow$ get_best_cost($\mathcal{P}$)
4: **while** *budget*$\neq 0$ **do**
5: $\quad\mathcal{P}_p \leftarrow$ tournament(2, $\mathcal{P}$) ▷ population of parents
6: $\quad\mathcal{P}_c \leftarrow$ SBX_crossover($\mathcal{P}_p$) ▷ population of children
7: $\quad\mathcal{P}_c \leftarrow$ polynomial_mutation($\mathcal{P}_c$)
8: $\quad$parallel_simulation($\mathcal{P}_c$)
9: $\quad\mathcal{P} \leftarrow$ elitist_replacement($\mathcal{P}$, $\mathcal{P}_c$, N)
10: $\quad$($\boldsymbol{x}_{min}$, y_{min}) $\leftarrow$ get_best_cost($\mathcal{P}$)
11: **end while**
12: **return** $\boldsymbol{x}_{min}$, y_{min}

Simulations were performed in parallel as they were the most computationally expensive part of the process (13 seconds on 1 computational core). The budget for the search was set to 12 hours on 1 computational node made of 18 Intel Xeon Gold 5220 cores proceeding from Grid5000, a large-scale testbed with a focus on parallel and distributed computing [30]. The population size was set to 126 in order to follow the general guidance given in [28] and to minimise the number of idle cores when simulating a population.

4.3 Sensitivity analysis applying perturbations on the optimal plans

Figures 2 and 3 (main text) present the optimal plans obtained after minimisation by age and by location, respectively. We also measured how variations in the optimised decision

variable would affect the objective functions (numbers of deaths and YLLs). To do this, we set a maximum allowed number of additional deaths or YLLs compared the optimum obtained under each configuration (Δobj). We then determined the alterations of the mixing factors that would:

1. cause an increase of Δobj in the objective function and
2. maintain the condition of herd immunity.

The thin black bars on Figures 2 and 3 represent the greatest perturbations allowed. These perturbations were applied to one mixing factor at a time.

5 Additional results

5.1 Effect of increased mixing on deaths and YLLs

We explored the effect of increasing mixing as compared to the optimal mitigation plans obtained using contact mitigation by age. That is, we applied a minimum bound b to the age-specific mixing factors such that the modified mixing profile could be described as $\{max(m_i^*, b)\}_{i\in\{1,...,16\}}$, where $\{m_i^*\}_{i\in\{1,...,16\}}$ represents the optimal (reference) solution originally obtained in the main analysis using $b = 0$. Figure S11 shows the results of this analysis in terms of predicted total numbers of COVID-19-related deaths and YLLs occurring after 1 August 2020 when considering $0 \leq b \leq .5$. Note that no additional optimisation was run for this exercise such that the predictions presented here were not optimal solutions. Recovered individuals were assumed to have persistent immunity in this analysis.

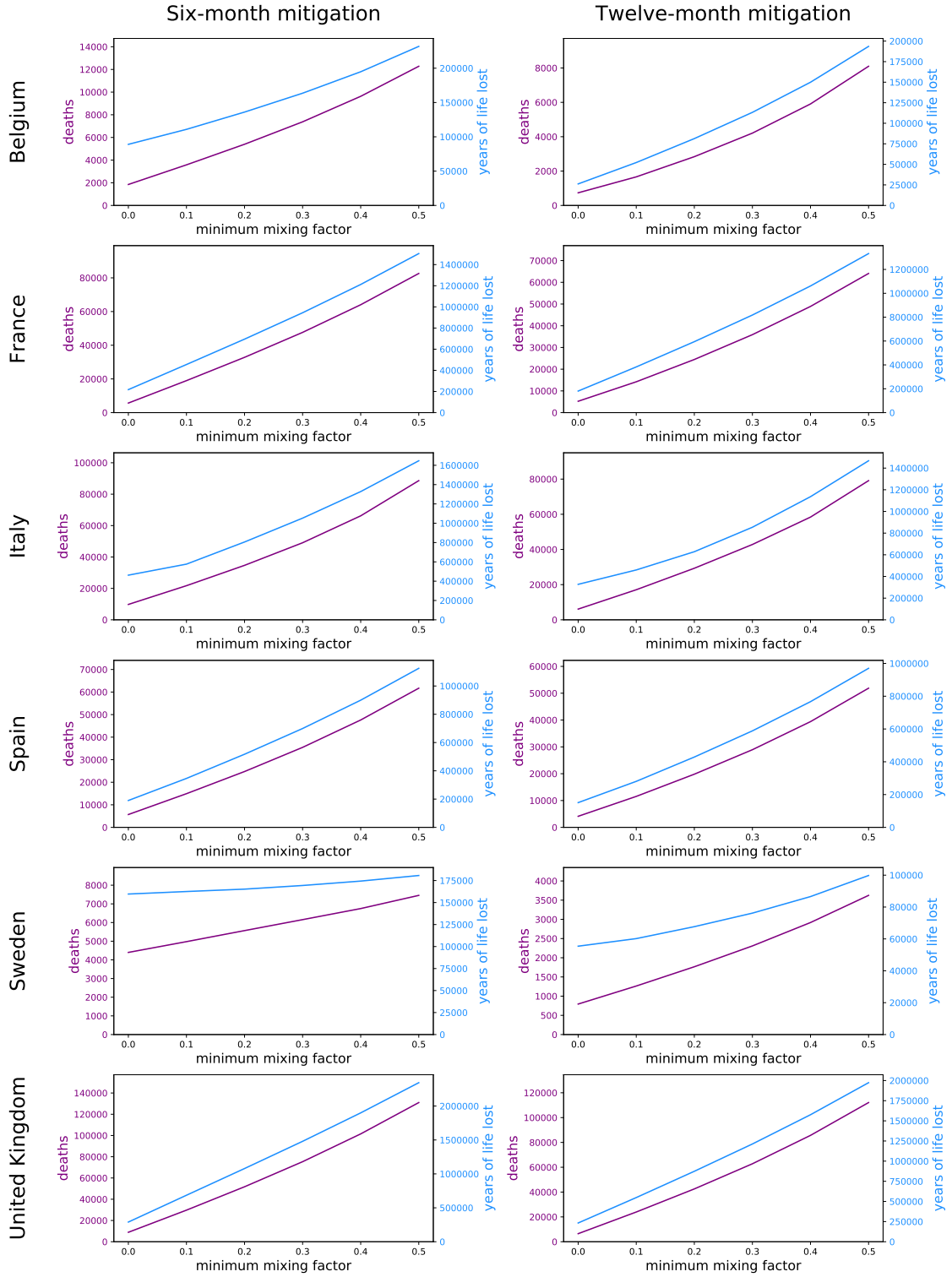

Figure S11. Impact of increasing mixing compared to the optimal strategies. The minimum mixing factor is the variable b described above. The purple line represents the total number of COVID-19-related deaths occurring after 1 Aug 2020 using the reference solution of the optimisation by age minimising deaths. The blue line represents the total number of COVID-19-related YLLs occurring after 1 Aug 2020 using the reference solution of the optimisation by age minimising YLLs.

5.2 Contact matrices resulting from the optimisation

The main text presents the optimisation results in terms of age-specific or location-specific mixing variables. Here we present the mixing matrices resulting from the optimised mixing factors. Figures S12 and S13 present the mixing matrices obtained under the different configurations when running the optimisation processes by ages and by location, respectively.

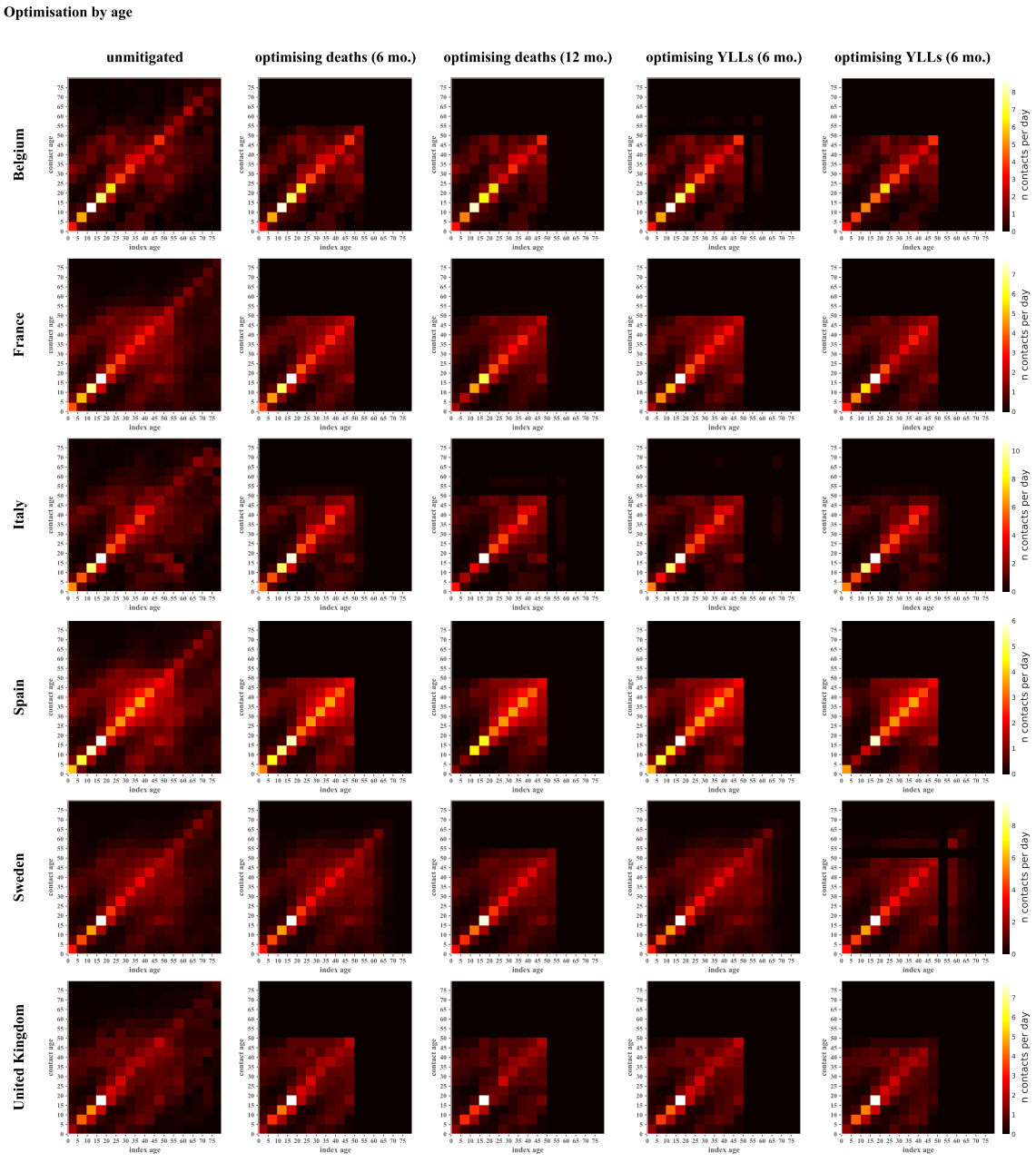

Figure S12. Age-specific contact matrices obtained from the optimisations by age.

Optimisation by location

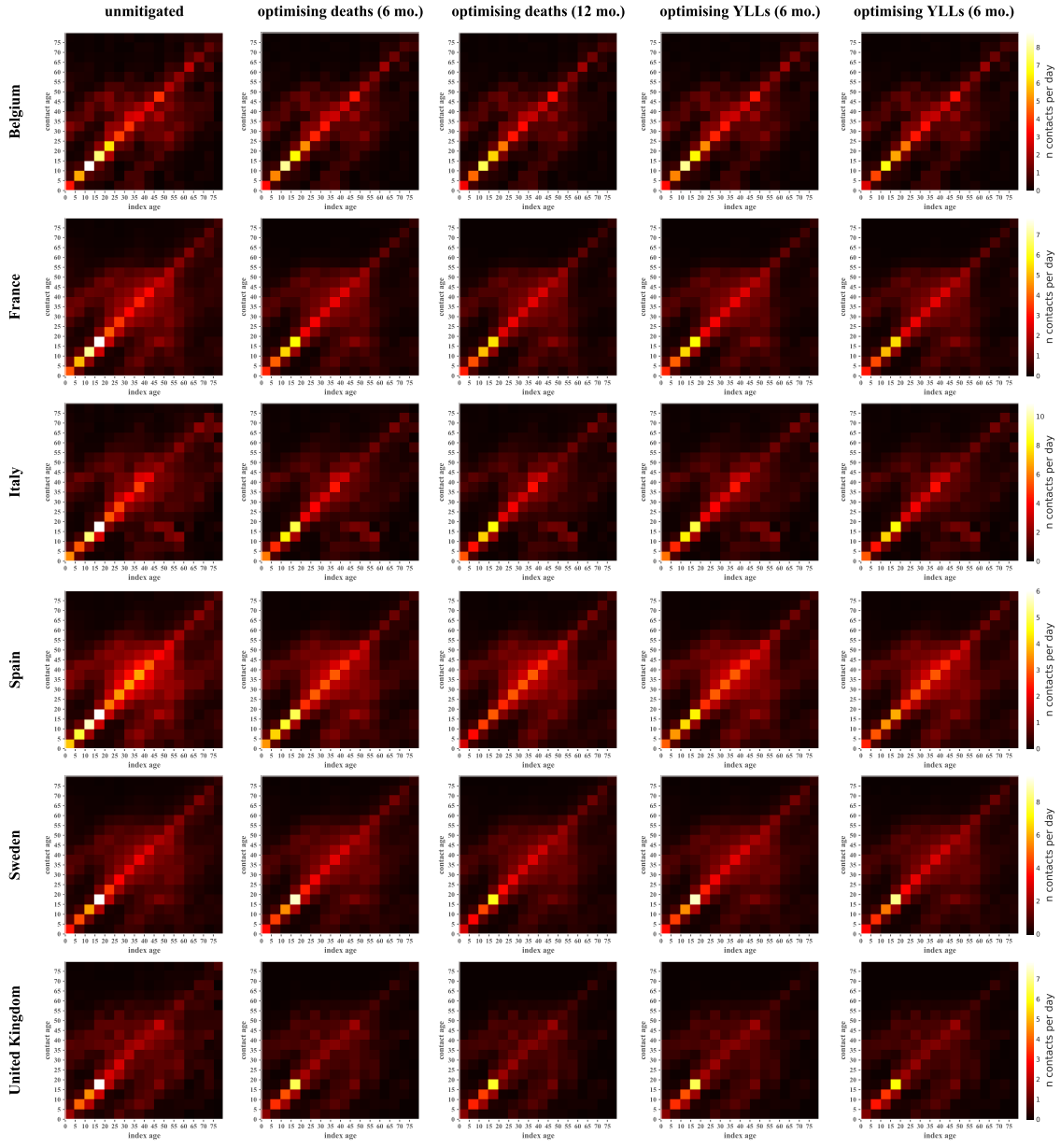

Figure S13. Age-specific contact matrices obtained from the optimisations by location.

5.3 Estimates of proportions of recovered individuals under optimised scenarios

Figure S14 presents the predicted proportion of recovered individuals over time under the optimised scenarios of mitigation by age. Recovered individuals were assumed to have persistent immunity in this analysis.

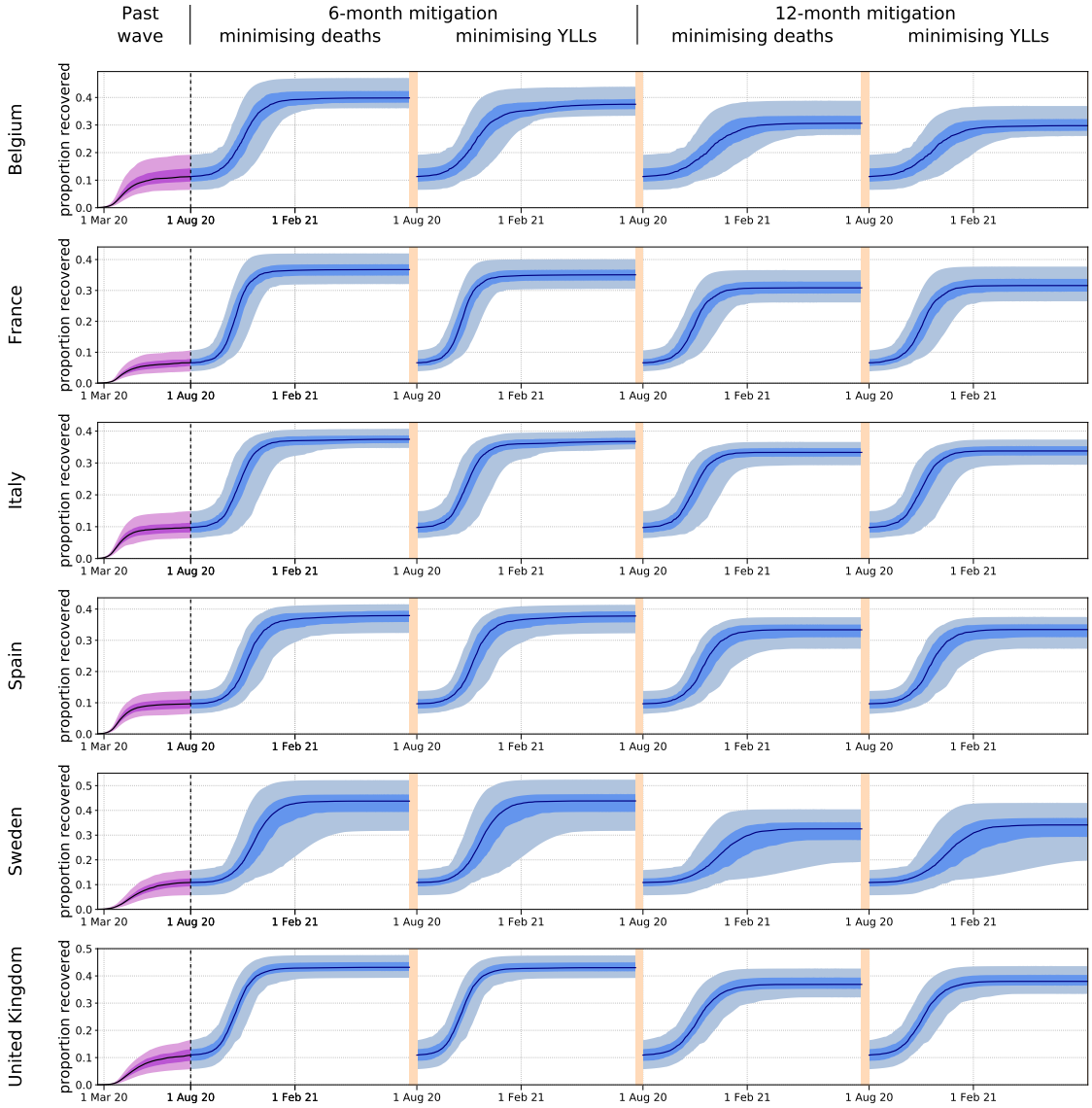

Figure S14. Posterior estimates of proportions of recovered individuals over time. The first waves (past epidemics) are represented in purple while the predictions of the future epidemics are represented in blue. The future epidemics are those associated with the four different optimisation configurations: six- or 12-month mitigation minimising total number of deaths or years of life lost (YLLs). The light shades show the central 95% credible intervals, the dark shades show the central 50% credible intervals and the solid lines represent the median estimates.

Figure S15 shows the age-specific proportion of recovered individuals after the optimised mitigation phase for the different optimisation configurations. Since the optimisation was constrained by the fact that herd immunity had to be reached by the end of the mitigation phase, these proportions could also be interpreted as age-specific vaccine coverage that would lead to herd immunity using a 100% vaccine.

Figure S15. Age-specific proportions of recovered individuals at the end of Phase 2. Recovered individuals assumed to have persistent immunity. Simulations based on the maximum-likelihood parameter sets. YLLs: years of life lost.

5.4 Predicted numbers of deaths and YLLs with optimised mitigation by location

Table S8 presents the predicted numbers of COVID-19-related deaths and YLLs associated with the optimisation process by location. Recovered individuals were assumed to have persistent immunity in this analysis.

Country	Mitigation phase	Deaths before 1 Aug 2020 (thousands)		Deaths from 1 Aug 2020 (thousands)			YLL before 1 Aug 2020 (thousands)	YLL from 1 Aug 2020 (thousands)		
		Model prediction	WHO report	Unmitigated	Optimised			Unmitigated	Optimised	
					Minimising deaths	Minimising YLL			Minimising deaths	Minimising YLL
Belgium	6 mo.	4.6 (2.5-8.5)	9.8	22.3 (15.9-32.3)	15.3 (10.3-20.0)	15.2 (10.3-20.3)	108 (59-180)	447 (306-574)	318 (245-428)	315 (245-424)
	12 mo.				10.1 (6.0-16.4)	10.6 (6.3-17.1)			234 (149-382)	228 (146-372)
France	6 mo.	27.2 (15.9-43.7)	30.1	260.6 (201.3-334.6)	143.2 (101.7-205.2)	143.2 (101.7-205.3)	425 (250-683)	4053 (3309-4504)	2353 (1814-3030)	2353 (1814-3030)
	12 mo.				112.8 (70.1-142.3)	115.7 (71.9-146.0)			1967 (1301-2368)	1932 (1278-2328)
Italy	6 mo.	40.9 (26.5-65.5)	35.1	304.2 (227.8-398.2)	176.1 (140.0-242.2)	176.4 (140.1-242.7)	635 (440-1060)	4291 (3645-5172)	2734 (2274-3404)	2734 (2276-3405)
	12 mo.				134.4 (83.3-205.9)	135.8 (84.2-208.0)			2195 (1399-2991)	2180 (1391-2971)
Spain	6 mo.	32.4 (18.5-62.7)	28.5	189.5 (141.6-269.1)	109.8 (75.6-156.3)	111.0 (76.5-158.7)	512 (312-812)	2978 (2423-3526)	1878 (1331-2254)	1873 (1324-2231)
	12 mo.				98.3 (56.2-150.7)	99.0 (56.8-151.6)			1651 (1028-2179)	1647 (1023-2177)
Sweden	6 mo.	6.3 (2.7-10.6)	5.7	23.6 (11.6-35.9)	17.8 (11.6-28.6)	17.8 (11.6-28.6)	108 (54-166)	397 (197-547)	316 (218-439)	315 (218-438)
	12 mo.				12.9 (6.6-22.6)	13.4 (6.8-23.3)			244 (134-368)	240 (133-361)
United Kingdom	6 mo.	31.4 (15.3-53.1)	46.0	252.5 (189.3-324.3)	95.0 (74.6-138.8)	94.2 (75.1-141.9)	608 (304-987)	3985 (3111-4814)	1986 (1652-2380)	1983 (1657-2412)
	12 mo.				47.7 (32.9-73.3)	49.6 (34.2-76.0)			1307 (850-1692)	1281 (834-1659)

Table S8. Predicted numbers of deaths and years of life lost (Optimisation by location).
Optimisation by location under the assumption of persistent immunity. Numbers are presented in thousands of deaths and YLLs as median and central 95% credible intervals. YLLs: Years of life lost.

5.5 Hospital occupancy with optimised mitigation by location

Figure S16 presents the predicted daily number of beds occupied by COVID-19 patients over time under the optimised scenarios of mitigation by location. Recovered individuals were assumed to have persistent immunity in this analysis.

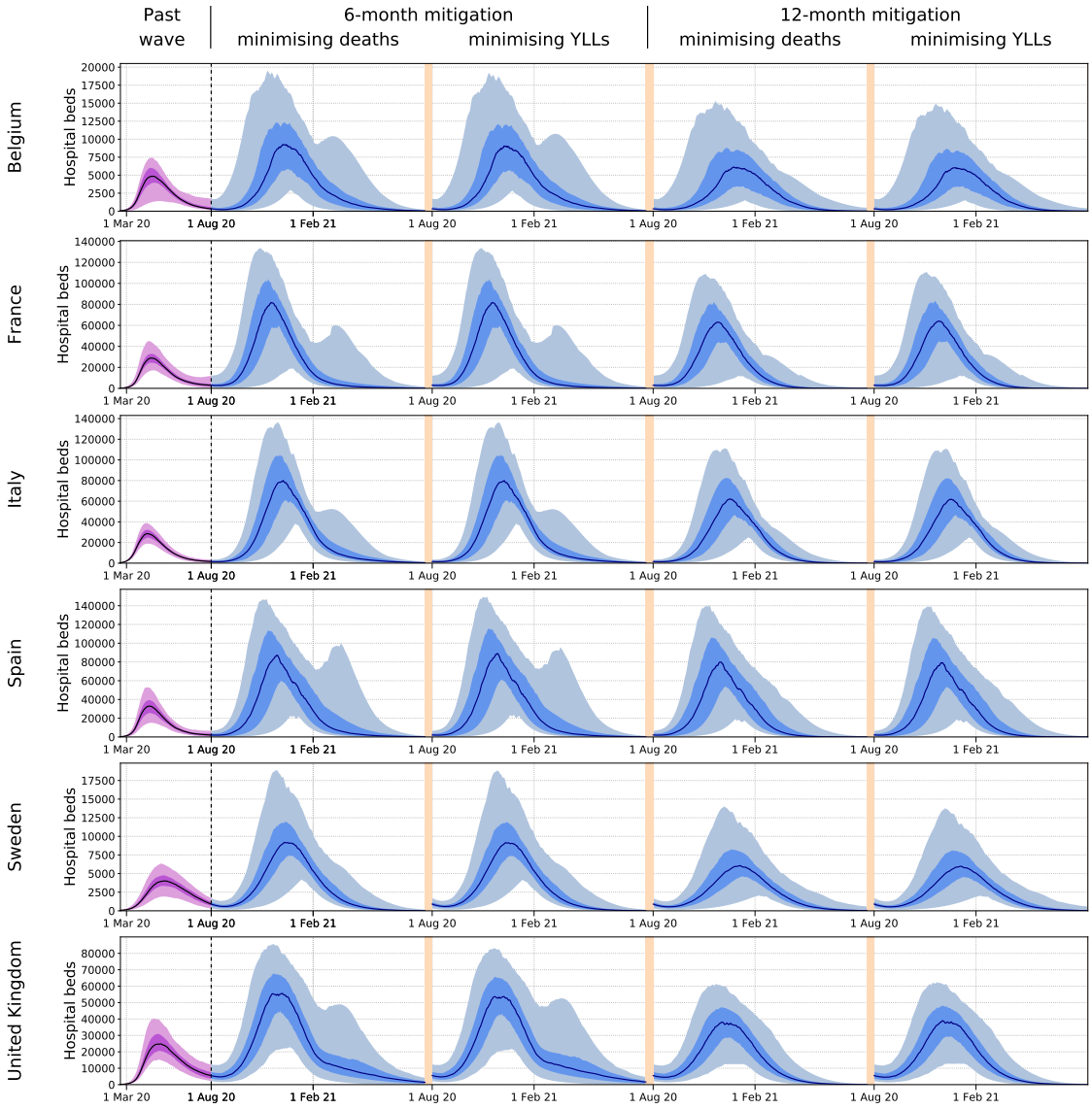

Figure S16. Hospital occupancy with mitigation optimised by location (assuming persistent immunity).
The first waves (past epidemics) are represented in purple while the predictions of the future epidemics are represented in blue. The future epidemics are those associated with the four different optimisation configurations: six- or 12-month mitigation minimising total number of deaths or years of life lost (YLLs). The light shades show the central 95% credible intervals, the dark shades show the central 50% credible intervals and the solid lines represent the median estimates.

5.6 Age-specific profiles of disease indicators over time

The following figures are the equivalent of Figure 3 (main text) under different configurations of optimisation. The configurations are indicated at the top of each figure and describe the type of mitigation (by age or by location), the duration of the mitigation phase (6 or 12 months) and the minimised indicator (deaths or YLLs).

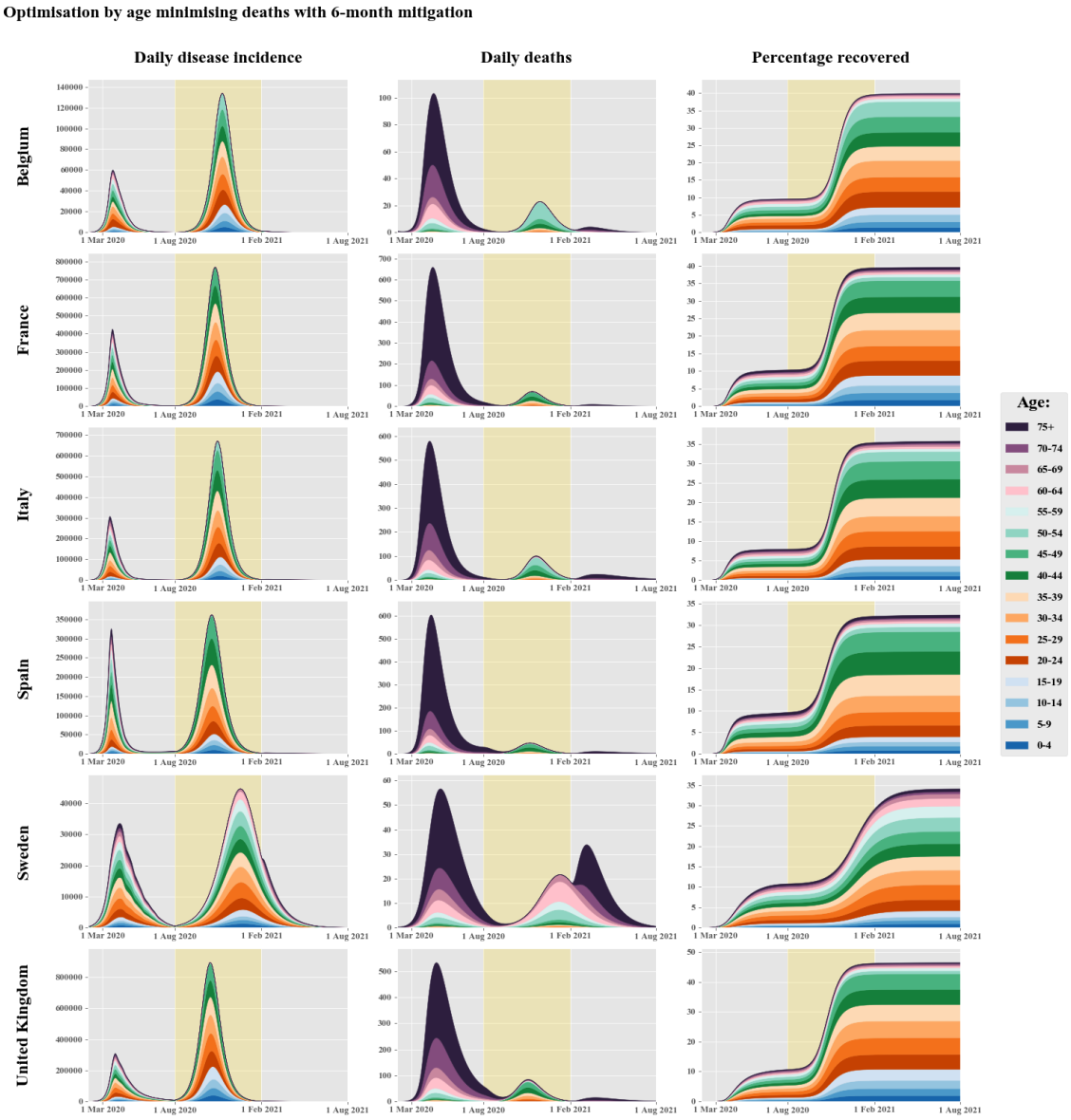

Figure S17. Age-specific profile of disease incidence, COVID-19-related deaths and proportion recovered over time
The yellow background indicates the intervention phase during which age-specific contacts were optimised. These projections were produced assuming that recovered individuals have persistent immunity against SARS-CoV-2 reinfection and using the maximum a posteriori estimates.

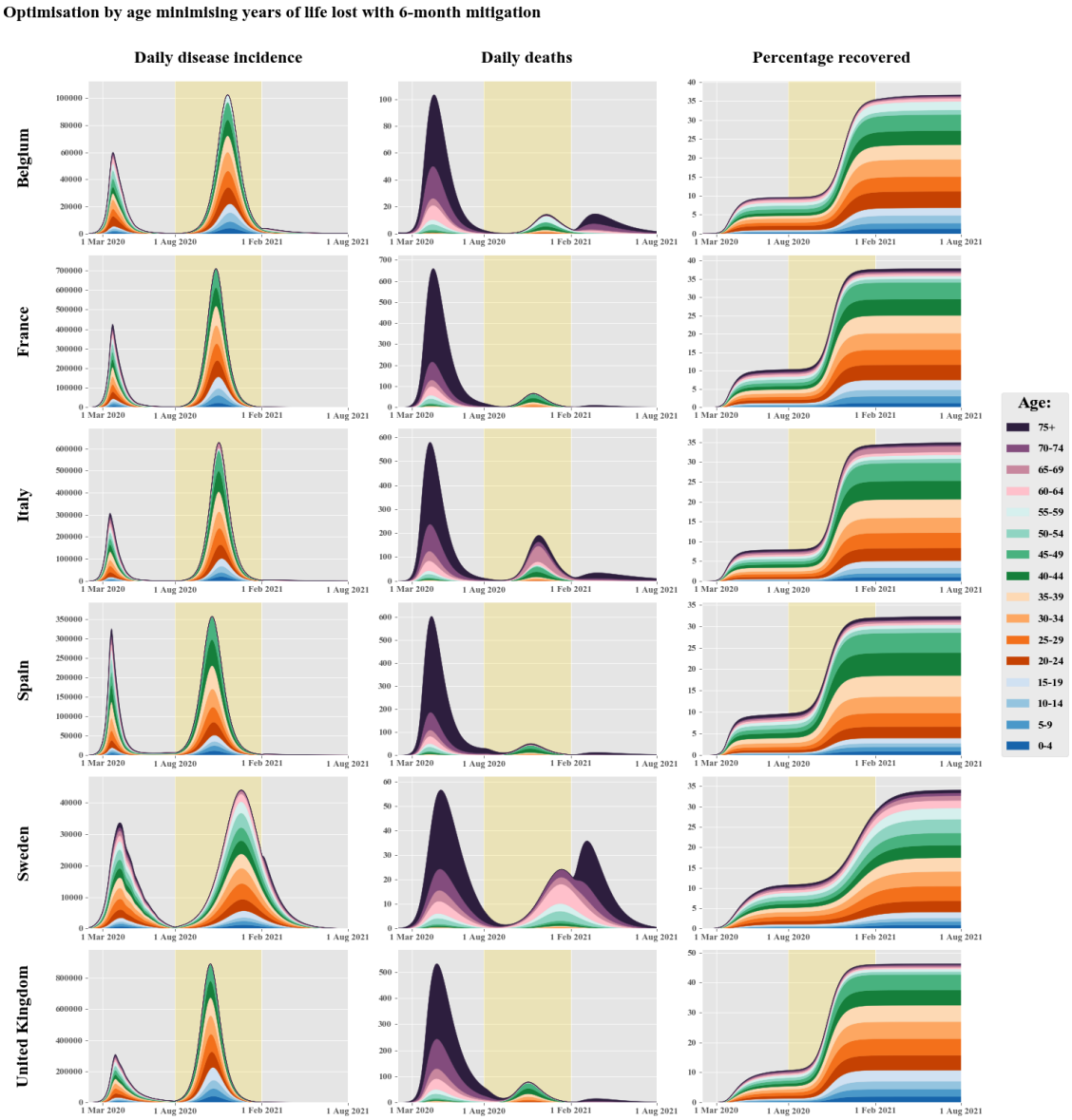

Figure S18. Age-specific profile of disease incidence, COVID-19-related deaths and proportion recovered over time

The yellow background indicates the intervention phase during which age-specific contacts were optimised. These projections were produced assuming that recovered individuals have persistent immunity against SARS-CoV-2 reinfection and using the maximum a posteriori estimates.

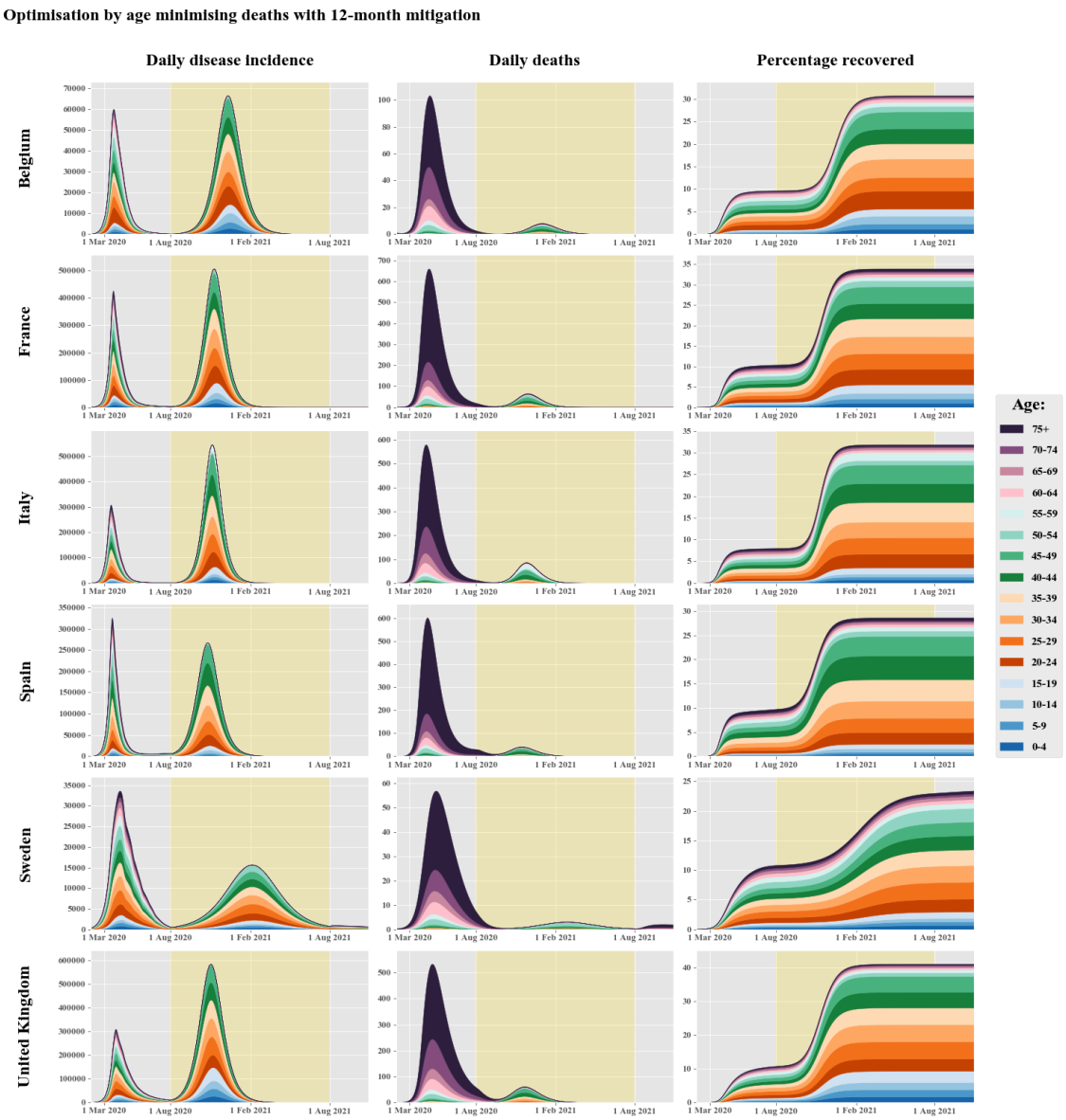

Figure S19. Age-specific profile of disease incidence, COVID-19-related deaths and proportion recovered over time
The yellow background indicates the intervention phase during which age-specific contacts were optimised. These projections were produced assuming that recovered individuals have persistent immunity against SARS-CoV-2 reinfection and using the maximum a posteriori estimates.

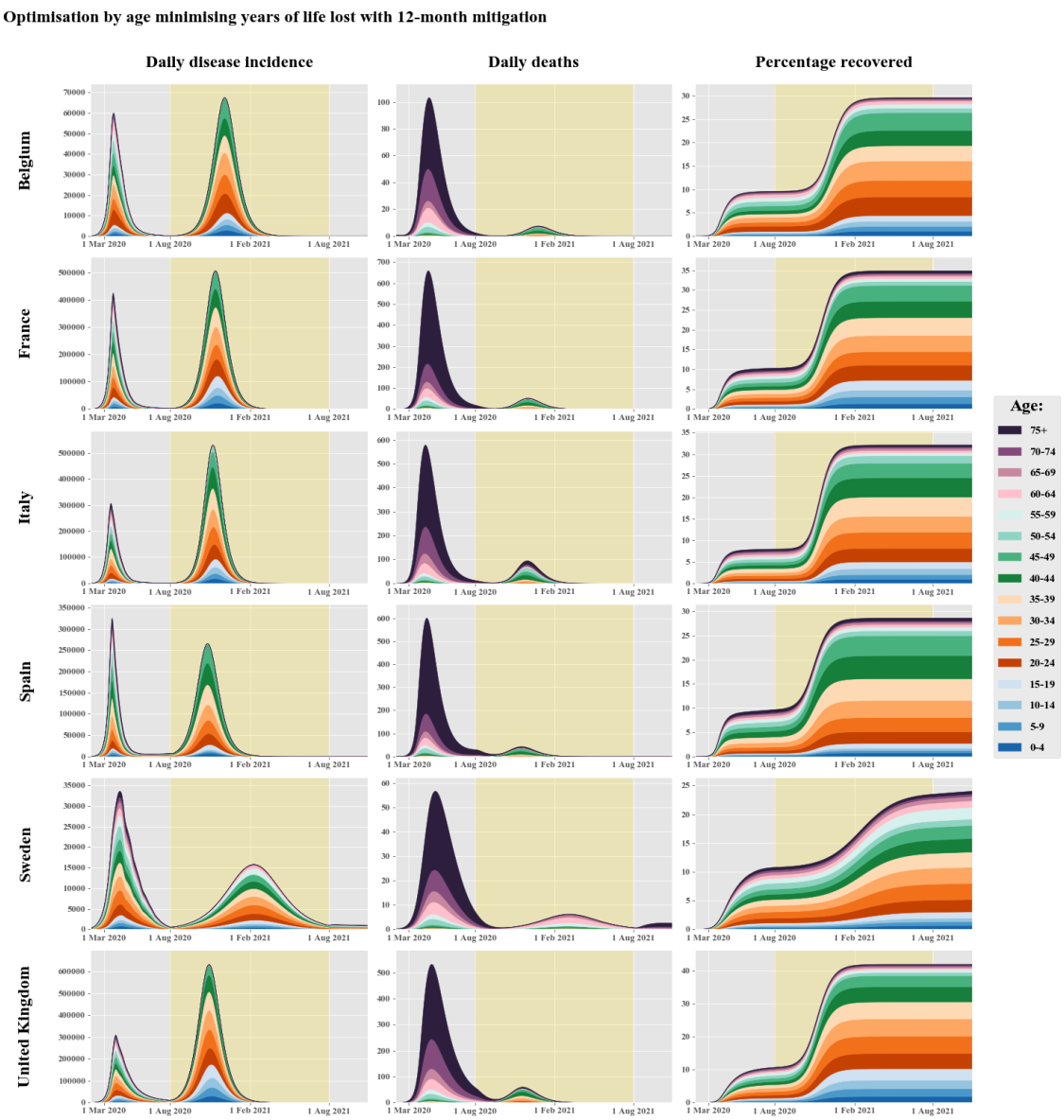

Figure S20. Age-specific profile of disease incidence, COVID-19-related deaths and proportion recovered over time

The yellow background indicates the intervention phase during which age-specific contacts were optimised. These projections were produced assuming that recovered individuals have persistent immunity against SARS-CoV-2 reinfection and using the maximum a posteriori estimates.

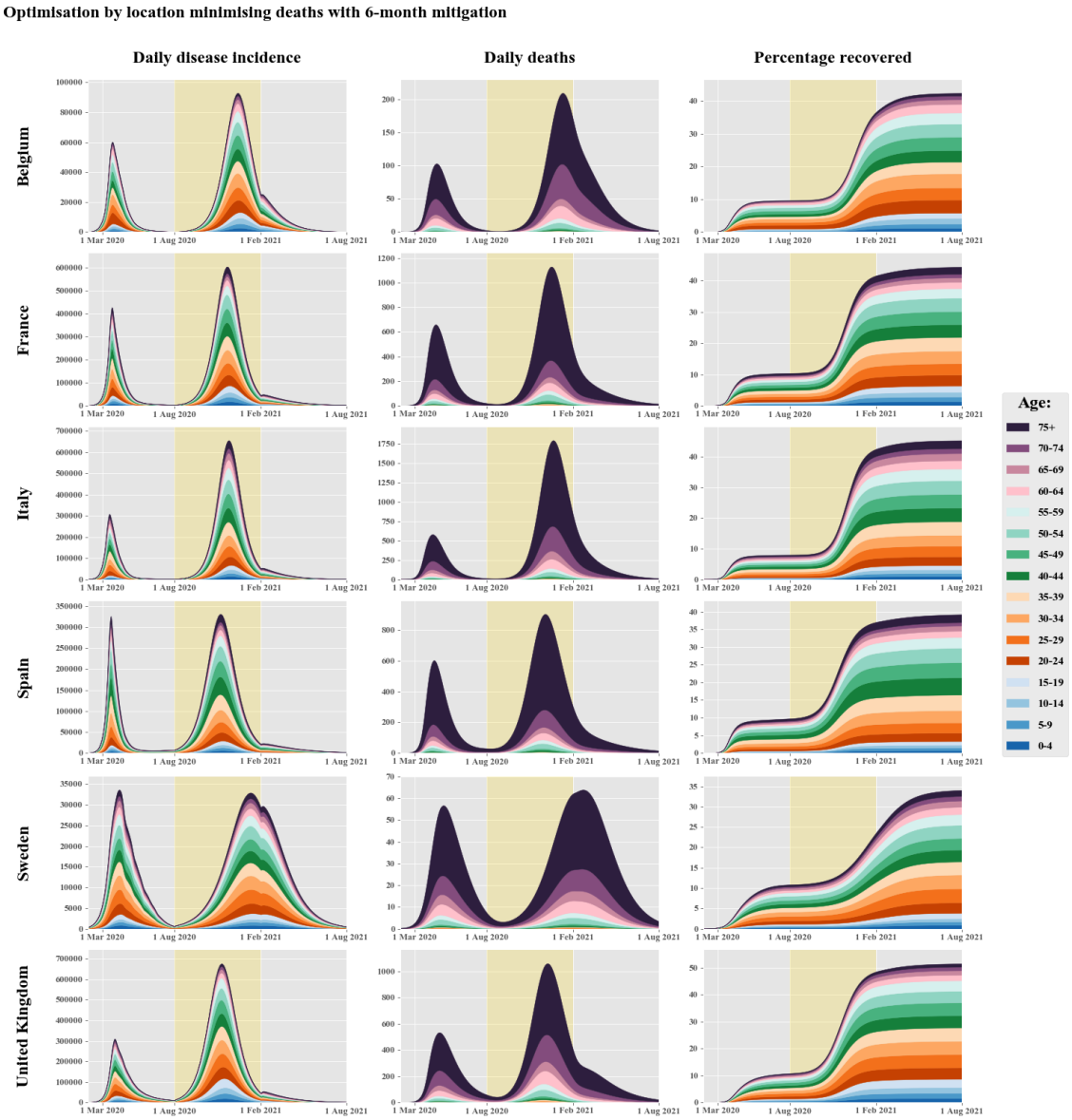

Figure S21. Age-specific profile of disease incidence, COVID-19-related deaths and proportion recovered over time
The yellow background indicates the intervention phase during which age-specific contacts were optimised. These projections were produced assuming that recovered individuals have persistent immunity against SARS-CoV-2 reinfection and using the maximum a posteriori estimates.

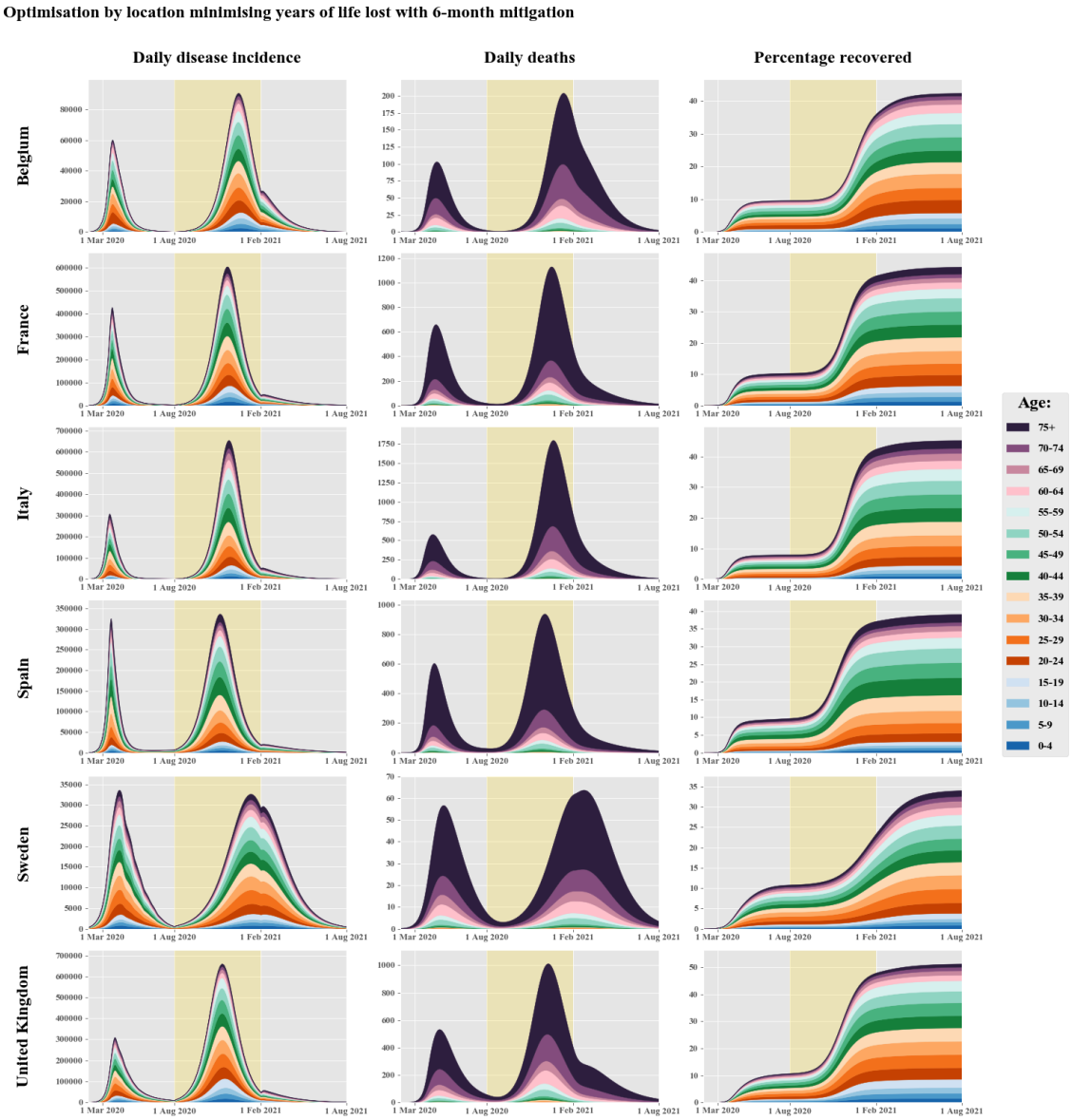

Figure S22. Age-specific profile of disease incidence, COVID-19-related deaths and proportion recovered over time

The yellow background indicates the intervention phase during which age-specific contacts were optimised. These projections were produced assuming that recovered individuals have persistent immunity against SARS-CoV-2 reinfection and using the maximum a posteriori estimates.

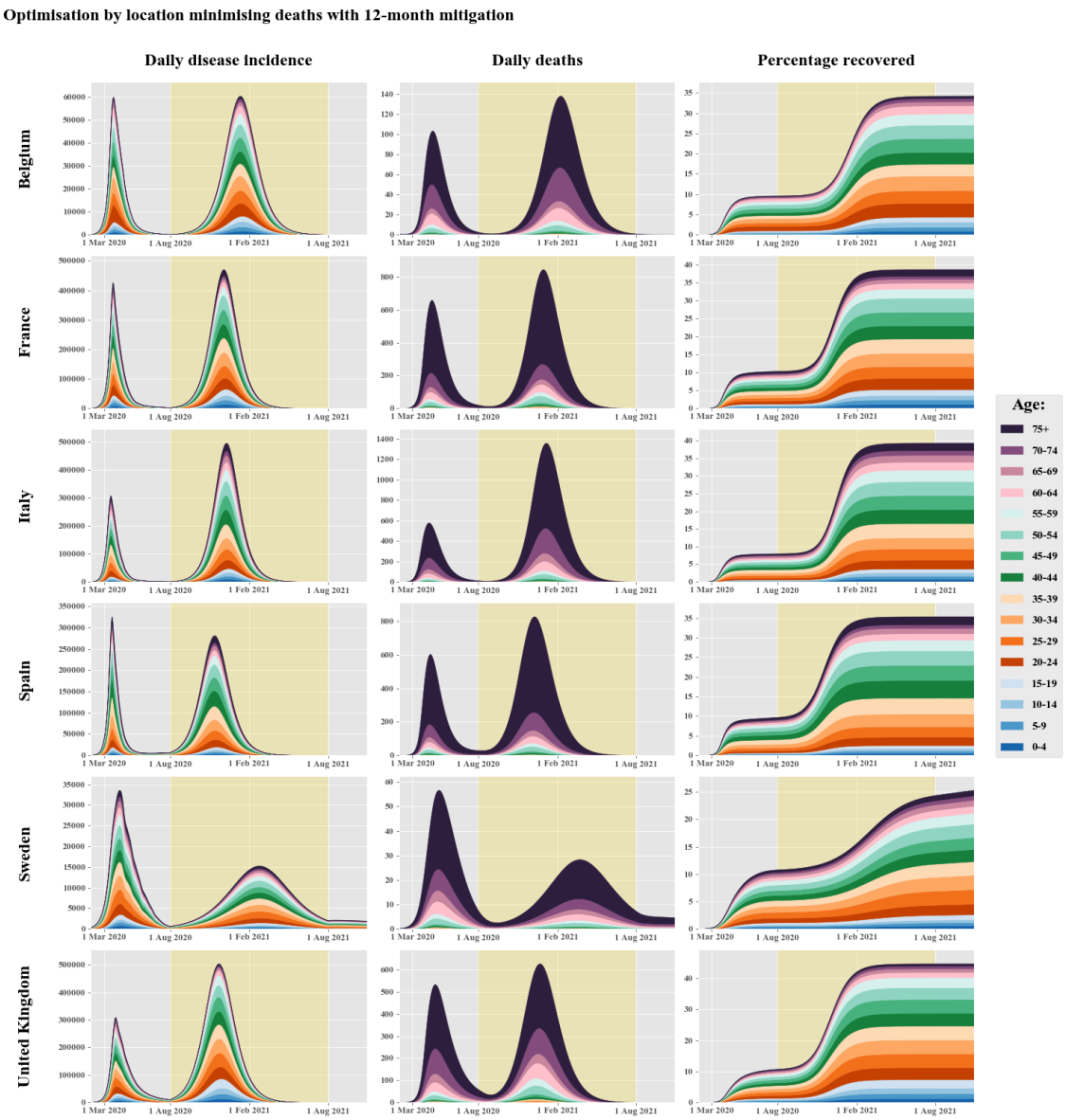

Figure S23. Age-specific profile of disease incidence, COVID-19-related deaths and proportion recovered over time
The yellow background indicates the intervention phase during which age-specific contacts were optimised. These projections were produced assuming that recovered individuals have persistent immunity against SARS-CoV-2 reinfection and using the maximum a posteriori estimates.

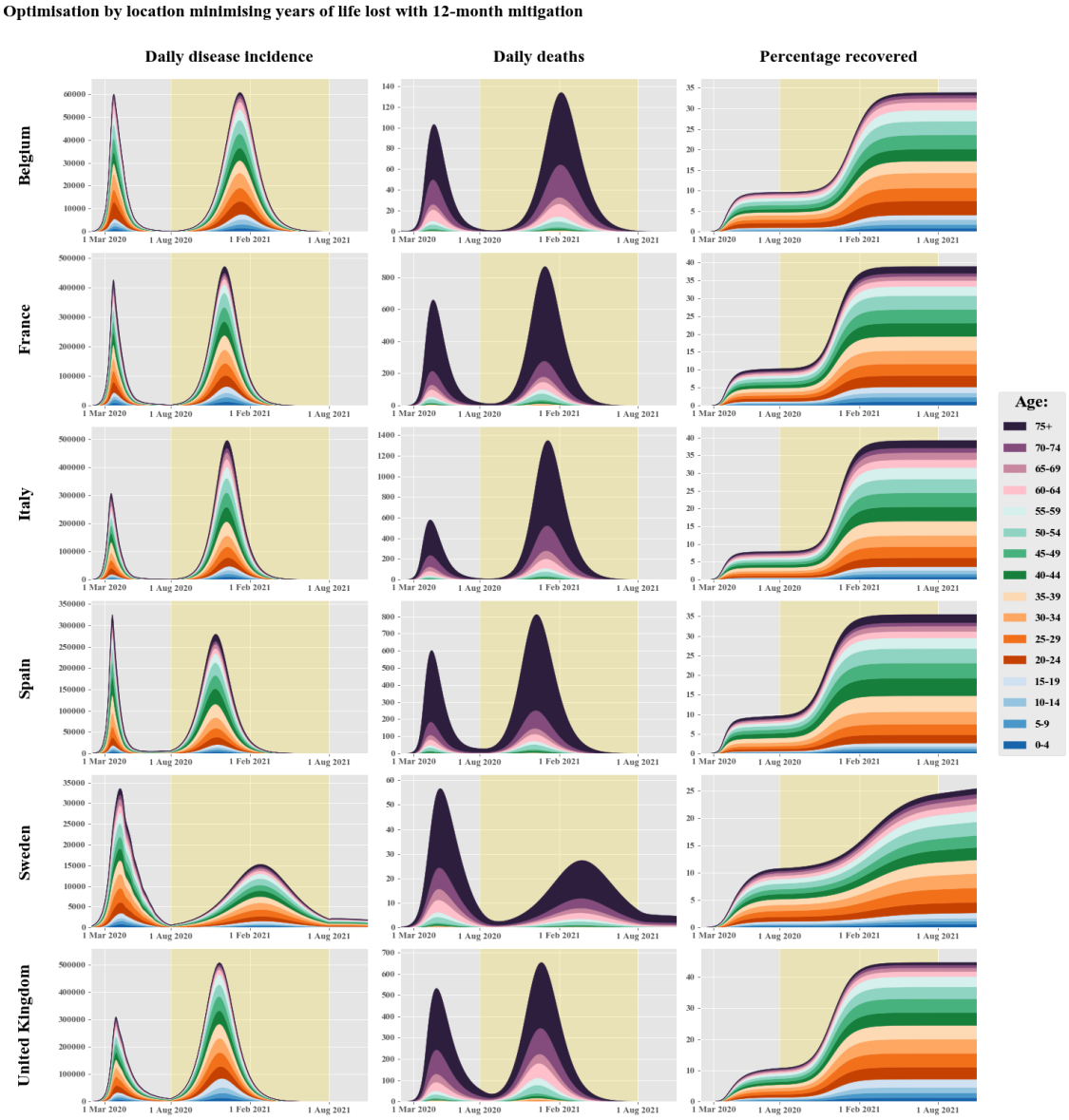

Figure S24. Age-specific profile of disease incidence, COVID-19-related deaths and proportion recovered over time
The yellow background indicates the intervention phase during which age-specific contacts were optimised. These projections were produced assuming that recovered individuals have persistent immunity against SARS-CoV-2 reinfection and using the maximum a posteriori estimates.

Figure S25. Age-specific profile of disease incidence, COVID-19-related deaths and proportion recovered over time
The yellow background indicates the intervention phase during which age-specific contacts were optimised. These projections were produced assuming that recovered individuals have persistent immunity against SARS-CoV-2 reinfection and using the maximum a posteriori estimates.

5.7 Epidemic trajectory using different assumptions for the profile of waning immunity.

The optimisations searches were all performed based on the assumption of persistent immunity for recovered individuals. However, we also ran epidemic simulations considering various assumptions of waning immunity while using the optimal mitigation plans obtained when assuming full immunity. We considered 5 different scenarios regarding post-infection immunity:

1. immunity against reinfection for an average of 6 months
2. immunity against reinfection for an average of 6 months and 50% reduction in disease severity
3. immunity against reinfection for an average of 24 months
4. immunity against reinfection for an average of 24 months and 50% reduction in disease severity
5. persistent immunity against reinfection

The 50% reduction in disease severity was modelled as a 50% reduction in the probability of presenting symptoms during repeat SARS-CoV-2 infections. The structure of the model implied that the same reduction also applies to the risk of hospitalisation and death. Figures S26, S27, S28 and Figure 7 (main text) show the predicted COVID-19 incidence, mortality and hospital occupancy over time for the different assumptions and considering the optimal plan obtained using different optimisation configurations.

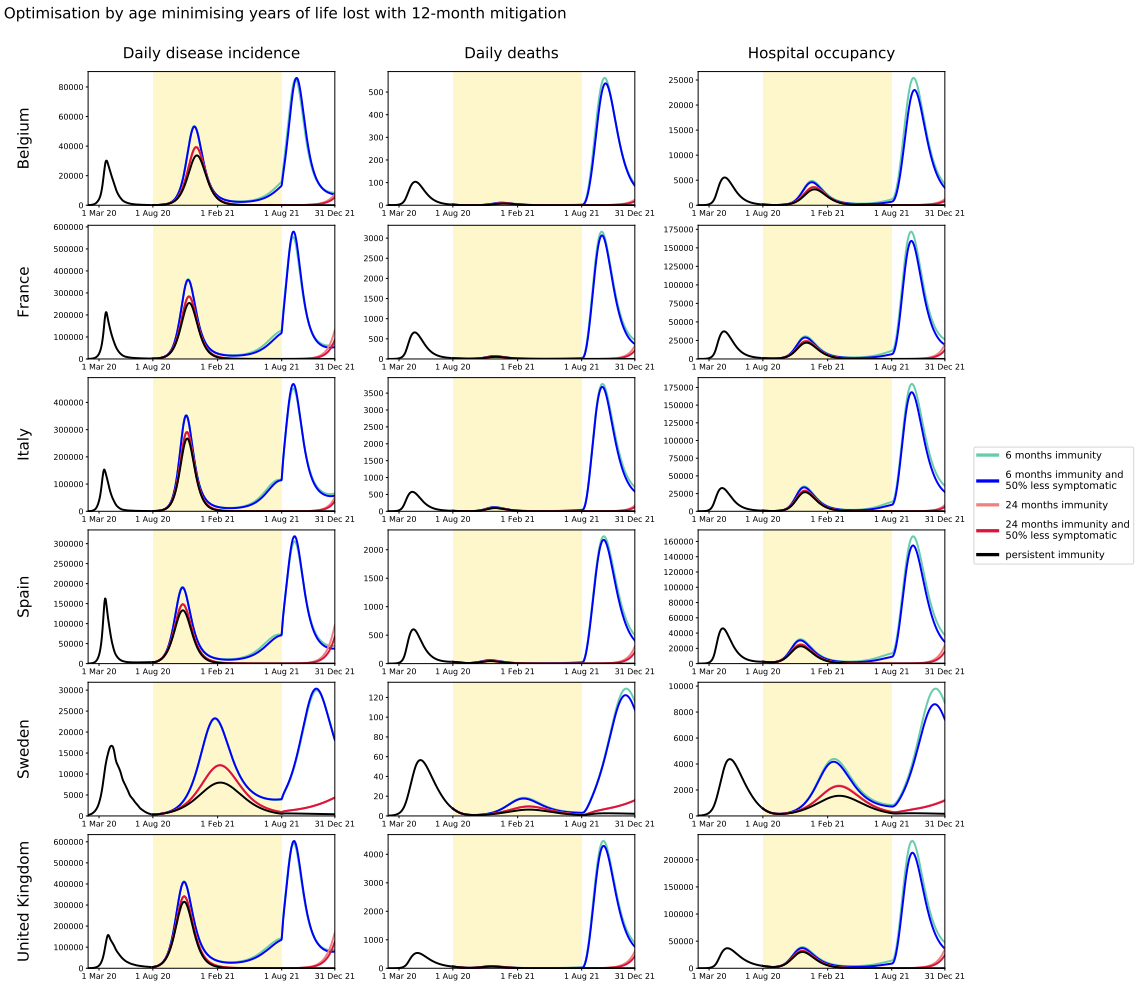

Figure S26. Predicted COVID-19 incidence, mortality and hospital occupancy over time under various assumptions of waning immunity.
The predictions were obtained using the maximum-likelihood parameter estimates and based on the 12-month contact mitigation by age minimising years of life lost (YLLs). The yellow background indicates the mitigation phase during which age-specific contacts were optimised. Five different assumptions were used to project the disease indicators: persistent immunity (black), 24-month immunity with and without 50% reduction in risk of symptoms for repeat infections (red and coral, respectively), 6-month immunity with and without 50% reduction in risk of symptoms for repeat infections (blue and turquoise, respectively).

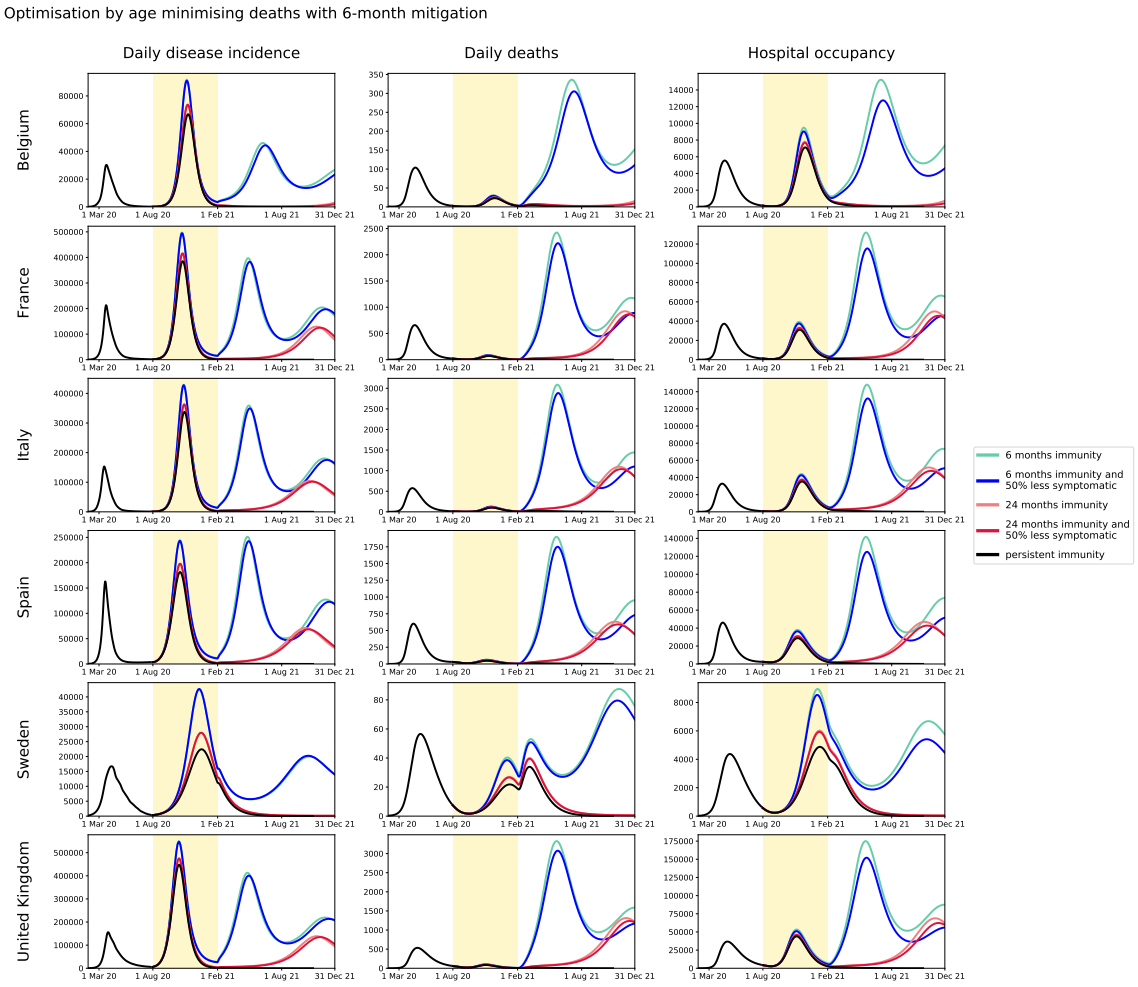

Figure S27. Predicted COVID-19 incidence, mortality and hospital occupancy over time under various assumptions of waning immunity.
The predictions were obtained using the maximum-likelihood parameter estimates and based on the 6-month contact mitigation by age minimising deaths. The yellow background indicates the mitigation phase during which age-specific contacts were optimised. Five different assumptions were used to project the disease indicators: persistent immunity (black), 24-month immunity with and without 50% reduction in risk of symptoms for repeat infections (red and coral, respectively), 6-month immunity with and without 50% reduction in risk of symptoms for repeat infections (blue and turquoise, respectively).

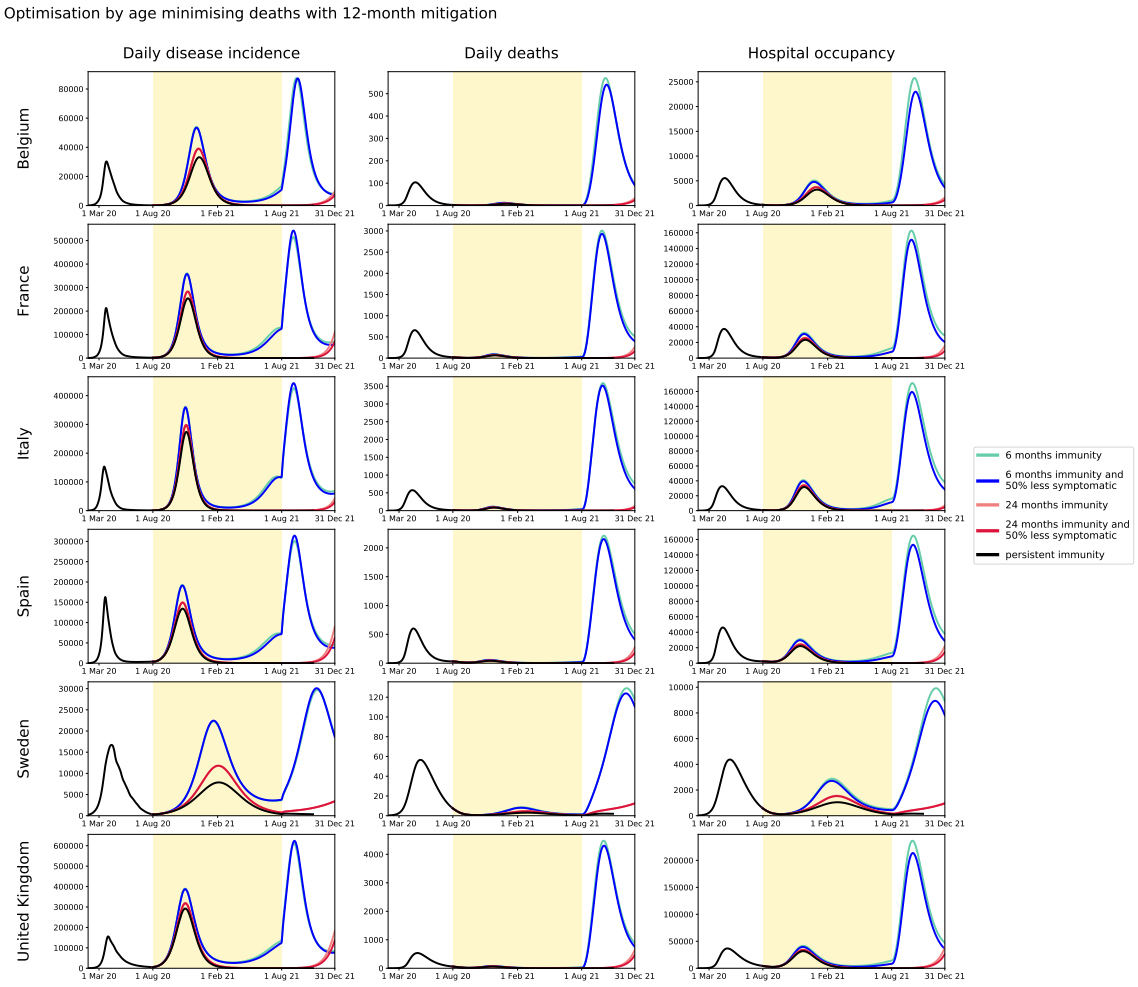

Figure S28. Predicted COVID-19 incidence, mortality and hospital occupancy over time under various assumptions of waning immunity.
The predictions were obtained using the maximum-likelihood parameter estimates and based on the 12-month contact mitigation by age minimising deaths. The yellow background indicates the mitigation phase during which age-specific contacts were optimised. Five different assumptions were used to project the disease indicators: persistent immunity (black), 24-month immunity with and without 50% reduction in risk of symptoms for repeat infections (red and coral, respectively), 6-month immunity with and without 50% reduction in risk of symptoms for repeat infections (blue and turquoise, respectively).

5.8 Epidemic trajectory under short-lived immunity applying mild mitigation after optimised phase.

We ran simulations under our most pessimistic assumption regarding waning immunity (6 month average duration and no effect on repeat disease severity), considering that mild contact mitigation was applied after the optimised phase. Figure 8 (main text) presents the predictions associated with the optimal age-mitigation plan obtained by minimising YLLs over a period of 6 months. The results of the other optimisation configurations are presented below.

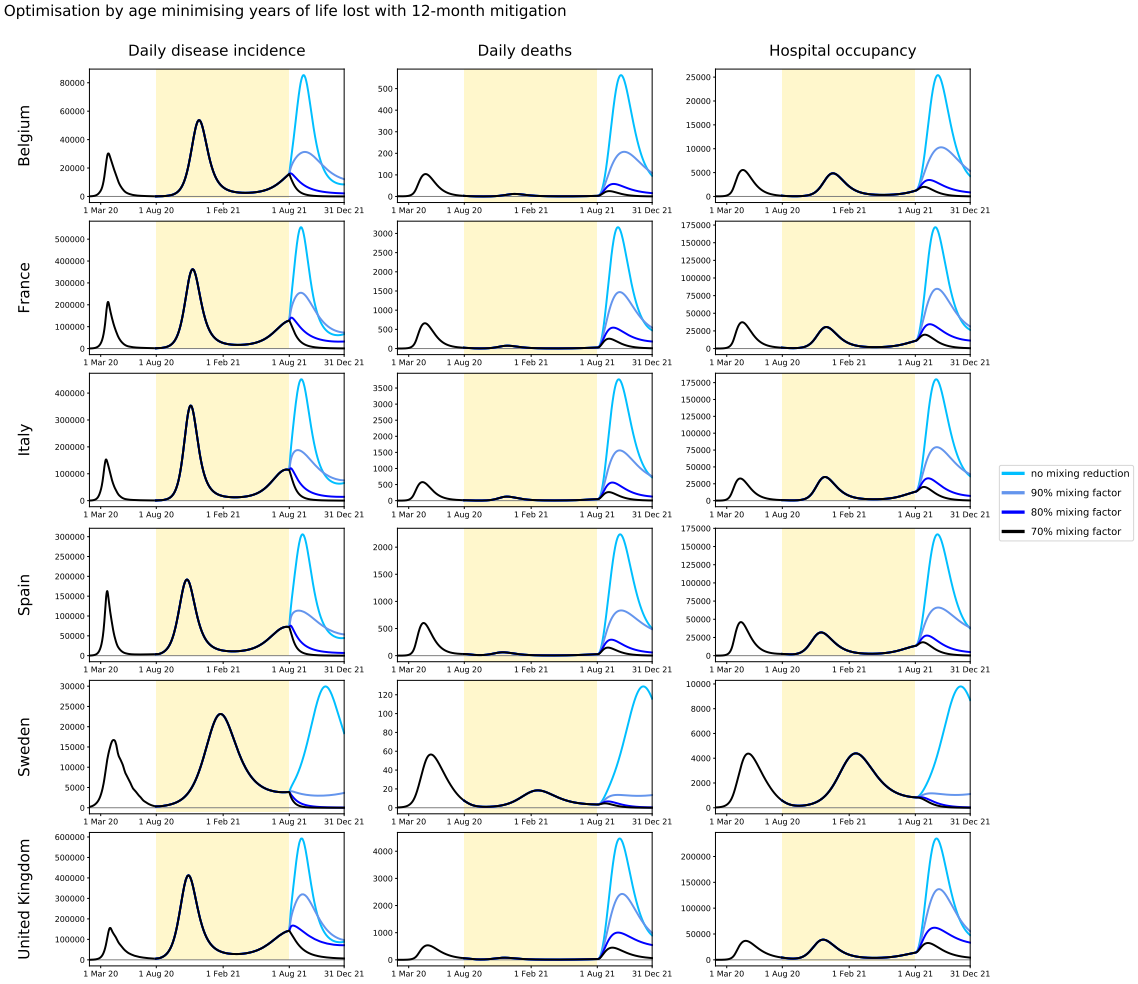

Figure S29. Predicted COVID-19 incidence, mortality and hospital occupancy over time with short-lived post-infection immunity and applying mild mixing reductions after the optimised phase.
The predictions were obtained using the maximum-likelihood parameter estimates and based on the 12-month contact mitigation by age minimising years of life lost (YLLs). The yellow background indicates the mitigation phase during which age-specific contacts were optimised. These predictions were obtained assuming 6-month average duration of immunity with no effect on the severity of repeat SARS-CoV-2 infections. The mixing factors were defined in the same way as during optimisation except that the same factor was applied to all age-groups. That is, a 90% mixing factor corresponds to a situation where every individual reduces their opportunity of contact by 10%.

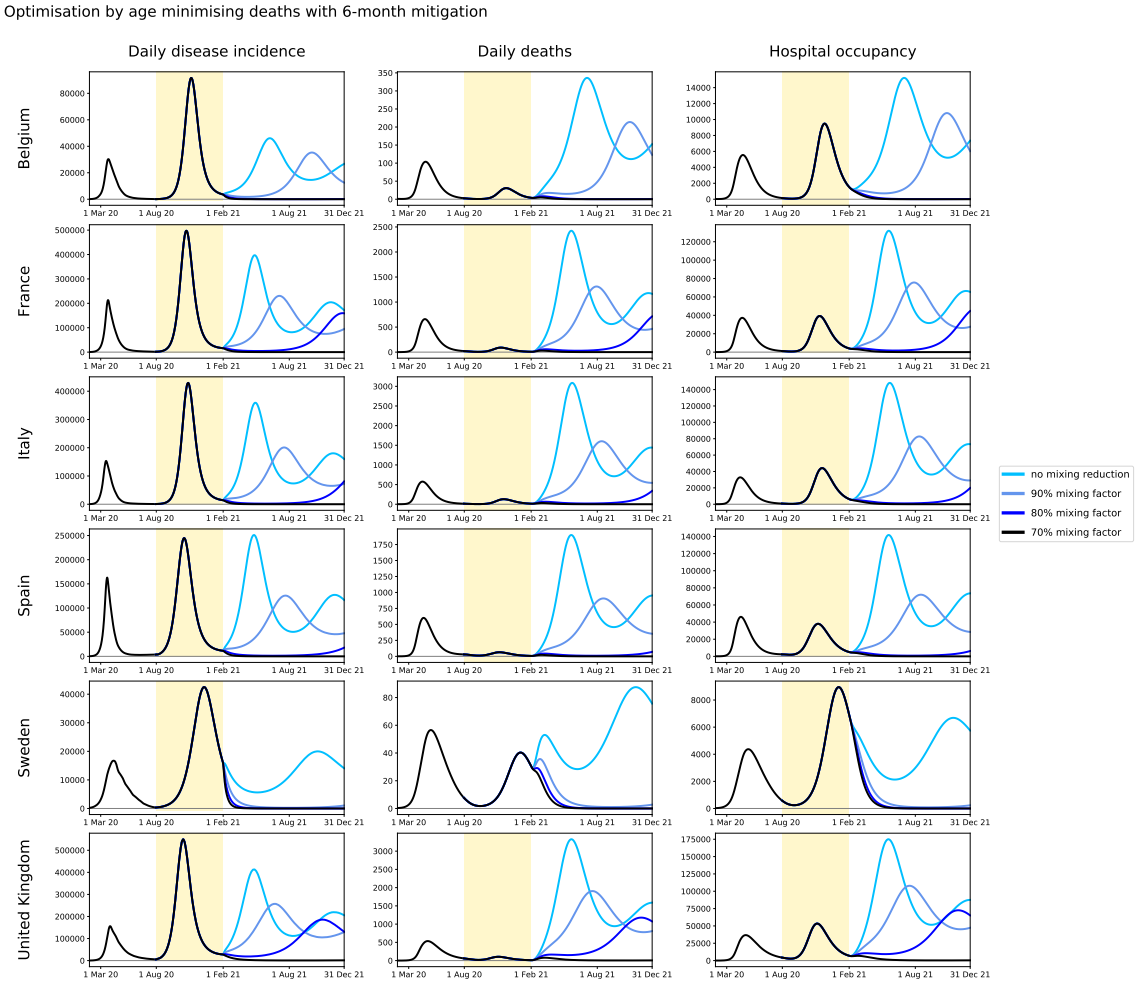

The predictions were obtained using the maximum-likelihood parameter estimates and based on the 6-month contact mitigation by age minimising years of life lost (deaths). The yellow background indicates the mitigation phase during which age-specific contacts were optimised. These predictions were obtained assuming 6-month average duration of immunity with no effect on the severity of repeat SARS-CoV-2 infections. The mixing factors were defined in the same way as during optimisation except that the same factor was applied to all age-groups. That is, a 90% mixing factor corresponds to a situation where every individual reduces their opportunity of contact by 10%.

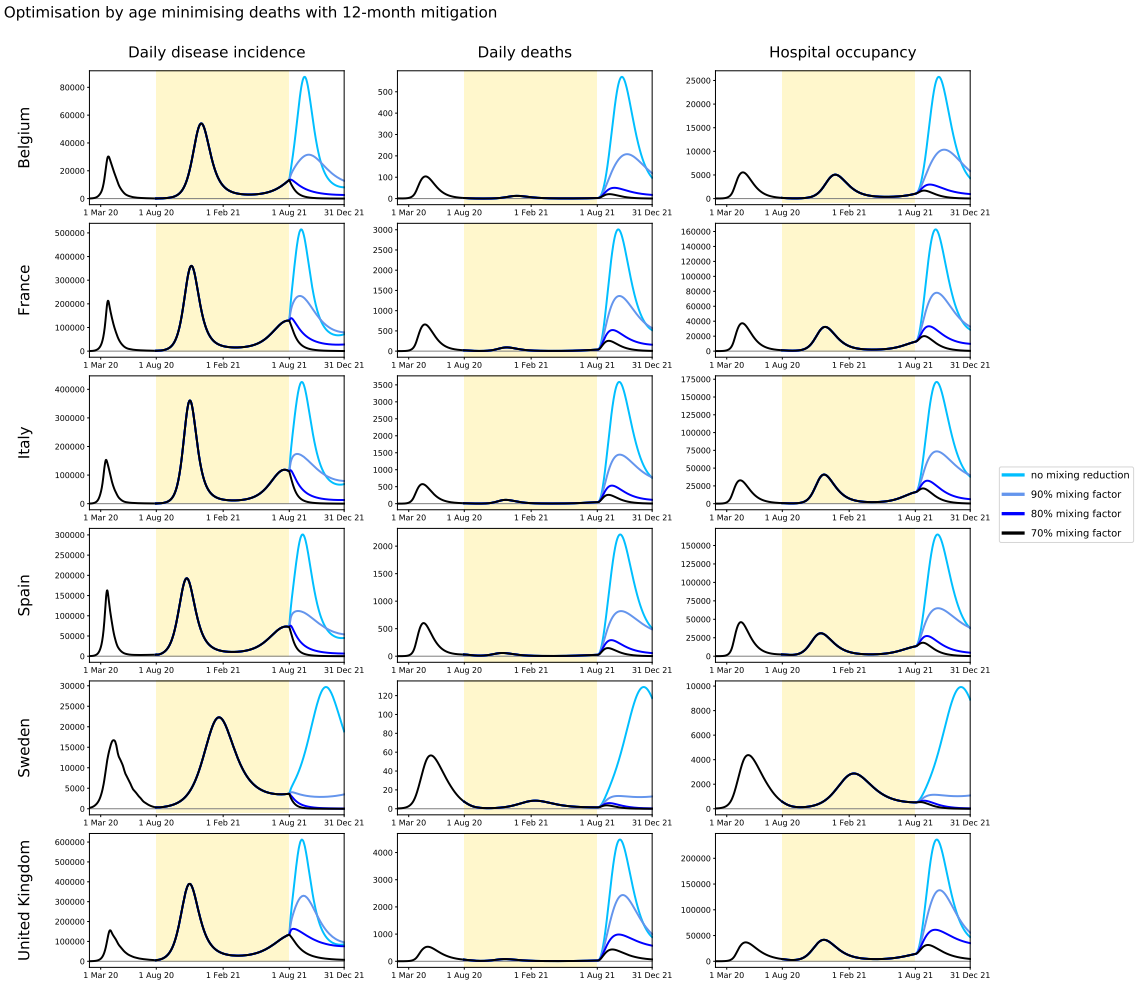

Figure S30. Predicted COVID-19 incidence, mortality and hospital occupancy over time with short-lived post-infection immunity and applying mild mixing reductions after the optimised phase.
The predictions were obtained using the maximum-likelihood parameter estimates and based on the 12-month contact mitigation by age minimising years of life lost (deaths). The yellow background indicates the mitigation phase during which age-specific contacts were optimised. These predictions were obtained assuming 6-month average duration of immunity with no effect on the severity of repeat SARS-CoV-2 infections. The mixing factors were defined in the same way as during optimisation except that the same factor was applied to all age-groups. That is, a 90% mixing factor corresponds to a situation where every individual reduces their opportunity of contact by 10%.

References

[1] Australian Tuberculosis Modelling Network, "AuTuMN Github repository."

[2] K. Prem, A. R. Cook, and M. Jit, "Projecting social contact matrices in 152 countries using contact surveys and demographic data," *PLoS Comput Biol*, vol. 13, no. 9, p. e1005697, 2017.

[3] M. Pollán, B. Pérez-Gómez, R. Pastor-Barriuso, J. Oteo, M. A. Hernán, M. Pérez-Olmeda, J. L. Sanmartín, A. Fernández-García, I. Cruz, N. Fernández de Larrea, M. Molina, F. Rodríguez-Cabrera, M. Martín, P. Merino-Amador, J. León Paniagua, J. F. Muñoz-Montalvo, F. Blanco, R. Yotti, R. Gutiérrez Fernández, S. Mezcua Navarro, J. F. Muñoz-Montalvo, M. Salinero Hernández, J. L. Sanmartín, M. Cuenca-Estrella, J. León Paniagua, P. Fernández-Navarro, A. Avellón, G. Fedele, J. Oteo Iglesias, M. T. Pérez Olmeda, M. E. Fernandez Martinez, F. D. Rodríguez-Cabrera, M. A. Hernán, S. Padrones Fernández, J. M. Rumbao Aguirre, J. M. Navarro Marí, B. Palop Borrás, A. B. Pérez Jiménez, M. Rodríguez-Iglesias, A. M. Calvo Gascón, M. L. Lou Alcaine, I. Donate Suárez, O. Suárez Álvarez, M. Rodríguez Pérez, M. Cases Sanchís, C. J. Villafáfila Gomila, L. Carbo Saladrigas, A. Hurtado Fernández, A. Oliver, E. Castro Feliciano, M. N. González Quintana, J. M. Barrasa Fernández, M. A. Hernández Betancor, M. Hernández Febles, L. Martín Martín, L. M. López López, T. Ugarte Miota, I. De Benito Población, M. S. Celada Pérez, M. N. Vallés Fernández, T. Maté Enríquez, M. Villa Arranz, M. Domínguez-Gil González, I. Fernández-Natal, G. Megías Lobón, J. L. Muñoz Bellido, P. Ciruela, A. Mas i Casals, M. Doladé Botías, M. A. Marcos Maeso, D. Pérez del Campo, A. Félix de Castro, R. Limón Ramírez, M. F. Elías Retamosa, M. Rubio González, M. S. Blanco Lobeiras, A. Fuentes Losada, A. Aguilera, G. Bou, Y. Caro, N. Marauri, L. M. Soria Blanco, I. del Cura González, M. Hernández Pascual, R. Alonso Fernández, N. Cabrera Castro, A. Tomás Lizcano, C. Ramírez Almagro, M. Segovia Hernández, N. Ascunce Elizaga, M. Ederra Sanz, C. Ezpeleta Baquedano, A. Bustinduy Bascaran, S. Iglesias Tamayo, L. Elorduy Otazua, R. Benarroch Benarroch, J. Lopera Flores, and A. Vázquez de la Villa, "Prevalence of SARS-CoV-2 in Spain (ENE-COVID): a nationwide, population-based seroepidemiological study," *The Lancet*, 2020.

[4] Ministerio de Sanidad (Spanish Ministry of Health), "Actualización nº115: enfermedad por SARS-CoV-2 (COVID-19) 24.05.2020."

[5] T. Chen, D. Wu, H. Chen, W. Yan, D. Yang, G. Chen, K. Ma, D. Xu, H. Yu, H. Wang, T. Wang, W. Guo, J. Chen, C. Ding, X. Zhang, J. Huang, M. Han, S. Li, X. Luo, J. Zhao, and Q. Ning, "Clinical characteristics of 113 deceased patients with coronavirus disease 2019: Retrospective study," *The BMJ*, 2020.

[6] UNESCO, "COVID-19 Impact on Education," 2020.

[7] Google, "COVID-19 Community Mobility Reports."

[8] J. Zhang, M. Litvinova, W. Wang, Y. Wang, X. Deng, X. Chen, M. Li, W. Zheng, L. Yi, X. Chen, Q. Wu, Y. Liang, X. Wang, J. Yang, K. Sun, I. M. Longini, M. E. Halloran, P. Wu, B. J. Cowling, S. Merler, C. Viboud, A. Vespignani, M. Ajelli, and H. Yu, "Evolving epidemiology and transmission dynamics of coronavirus disease 2019 outside Hubei province, China: a descriptive and modelling study," *The Lancet Infectious Diseases*, vol. 20, no. 7, 2020.

[9] S. A. Lauer, K. H. Grantz, Q. Bi, F. K. Jones, Q. Zheng, H. R. Meredith, A. S. Azman, N. G. Reich, and J. Lessler, "The Incubation Period of Coronavirus Disease 2019 (COVID-19) From Publicly Reported Confirmed Cases: Estimation and Application.," *Annals of Internal Medicine*, vol. 172, pp. 577–582, may 2020.

[10] Q. Li, X. Guan, P. Wu, X. Wang, L. Zhou, Y. Tong, R. Ren, K. S. Leung, E. H. Lau, J. Y. Wong, X. Xing, N. Xiang, Y. Wu, C. Li, Q. Chen, D. Li, T. Liu, J. Zhao, M. Liu, W. Tu, C. Chen, L. Jin, R. Yang, Q. Wang, S. Zhou, R. Wang, H. Liu, Y. Luo, Y. Liu, G. Shao, H. Li, Z. Tao, Y. Yang, Z. Deng, B. Liu, Z. Ma, Y. Zhang, G. Shi, T. T. Lam, J. T. Wu, G. F. Gao, B. J. Cowling, B. Yang, G. M. Leung, and Z. Feng, "Early transmission dynamics in Wuhan, China, of novel coronavirus-infected pneumonia," mar 2020.

[11] Q. Bi, Y. Wu, S. Mei, C. Ye, X. Zou, Z. Zhang, X. Liu, L. Wei, S. A. Truelove, T. Zhang, W. Gao, C. Cheng, X. Tang, X. Wu, Y. Wu, B. Sun, S. Huang, Y. Sun, J. Zhang, T. Ma, J. Lessler, and T. Feng, "Epidemiology and Transmission of COVID-19 in Shenzhen China: Analysis of 391 cases and 1,286 of their close contacts," *medRxiv*, p. 2020.03.03.20028423, mar 2020.

[12] X. He, E. H. Lau, P. Wu, X. Deng, J. Wang, X. Hao, Y. C. Lau, J. Y. Wong, Y. Guan, X. Tan, X. Mo, Y. Chen, B. Liao, W. Chen, F. Hu, Q. Zhang, M. Zhong, Y. Wu, L. Zhao, F. Zhang, B. J. Cowling, F. Li, and G. M. Leung, "Temporal dynamics in viral shedding and transmissibility of COVID-19," *Nature Medicine*, p. 2020.03.15.20036707, mar 2020.

[13] ISARIC, "ISARIC (International Severe Acute Respiratory and Emerging Infections Consortium) COVID-19 Report: 08 June 2020," tech. rep., 2020.

[14] N. G. Davies, P. Klepac, Y. Liu, K. Prem, M. Jit, and R. M. Eggo, "Age-dependent effects in the transmission and control of COVID-19 epidemics," *Nature Medicine*, pp. 1–7, jun 2020.

[15] R. Verity, L. C. Okell, I. Dorigatti, P. Winskill, C. Whittaker, N. Imai, G. Cuomo-Dannenburg, H. Thompson, P. G. Walker, H. Fu, A. Dighe, J. T. Griffin, M. Baguelin, S. Bhatia, A. Boonyasiri, A. Cori, Z. Cucunubá, R. FitzJohn, K. Gaythorpe, W. Green, A. Hamlet, W. Hinsley, D. Laydon, G. Nedjati-Gilani, S. Riley, S. van Elsland, E. Volz, H. Wang, Y. Wang, X. Xi, C. A. Donnelly, A. C. Ghani, and N. M. Ferguson, "Estimates of the severity of coronavirus disease 2019: a model-based analysis," *The Lancet Infectious Diseases*, vol. 20, pp. 669–677, mar 2020.

[16] WHO, "WHO COVID-19 dashboard."

[17] Sciensano, "COVID-19 Belgium Epidemiological Situation."

[18] Santé Publique France, "Données hospitalières relatives à l'épidémie de COVID-19."

[19] Dipartimento della Protezione Civile, "Emergenza Coronavirus: la risposta nazionale."

[20] Svenska Intensivvårdsregistret (Swedish Intensive Care Registry), "Covid-19 på svenska intensivvårdsavdelningar."

[21] UK Government, "Coronavirus (COVID-19) in the UK."

[22] S. Herzog, J. D. Bie, S. Abrams, I. Wouters, E. Ekinci, L. Patteet, A. Coppens, S. D. Spiegeleer, P. Beutels, P. V. Damme, N. Hens, and H. Theeten, "Seroprevalence of IgG antibodies against SARS coronavirus 2 in Belgium: a prospective cross-sectional study of residual samples," *medRxiv*, 2020.

[23] P. Gallian, B. Pastorino, P. Morel, J. Chiaroni, L. Ninove, and X. de Lamballerie, "Lower prevalence of antibodies neutralizing SARS-CoV-2 in group O French blood donors," *Antiviral Research*, 2020.

[24] L. L. Sabbadini, "Primi risultati dell'indagine di sieroprevalenza SARS-CoV-2," tech. rep., 2020.

[25] N. Roxhed, A. Bendes, M. Dale, C. Mattsson, L. Hanke, T. Dodig-Crnkovic, M. Christian, B. Meineke, S. Elsasser, J. Andrell, S. Haverall, C. Thalin, C. Eklund, J. Dillner, O. Beck, C. E. Thomas, G. McInerney, M.-G. Hong, B. Murrell, C. Fredolini, and J. M. Schwenk, "A translational multiplex serology approach to profile the prevalence of anti-SARS-CoV-2 antibodies in home-sampled blood," *medRxiv*, 2020.

[26] Biobank, "UK Biobank SARS-CoV-2 Serology Study," tech. rep., 2020.

[27] H. Ward, C. Atchison, M. Whitaker, K. Ainslie, J. Elliott, L. Okell, R. Redd, D. Ashby, C. Donnelly, W. Barclay, A. Darzi, G. Cooke, S. Riley, and P. Elliott, "Antibody prevalence for SARS-CoV-2 following the peak of the pandemic in England: REACT2 study in 100,000 adults," *Preprint*, 2020.

[28] E. G. Talbi, *Metaheuristics: From Design to Implementation*. Wiley Series on Parallel and Distributed Computing, Wiley, 2009.

[29] G. Briffoteaux, R. Ragonnet, M. Mezmaz, N. Melab, and D. Tuyttens, "Evolution control for parallel ann-assisted simulation-based optimization application to tuberculosis transmission control," *Future Generation Computer Systems*, vol. 113, pp. 454 – 467, 2020.

[30] R. Bolze *et al.*, "Grid'5000: A large scale and highly reconfigurable experimental grid testbed," *The International Journal of High Performance Computing Applications*, vol. 20, no. 4, pp. 481–494, 2006.